Ore Geology Reviews 142 (2022) 104728

Contents lists available at ScienceDirect

Ore Geology Reviews

journal homepage: www.elsevier.com/locate/oregeorev

Origin of the Shanggong gold deposit, the southern margin of the North China Craton: Constraints from Rb-Sr ages of sericite, and trace elements and sulfur isotope of pyrite

Lei Meng [a,b,c], Caiyun Lan [d], Qiang Zhan [b,c], Qiang Wu [b,c], Taiping Zhao [b,c,*]

[a] State Key Laboratory of Ore Deposit Geochemistry, Institute of Geochemistry, Chinese Academy of Sciences, Guiyang 550081, China
[b] Key Laboratory of Mineralogy and Metallogeny, Guangzhou Institute of Geochemistry, Chinese Academy of Sciences, Guangzhou 510640, China
[c] CAS Center for Excellence in Deep Earth Science, Guangzhou 510640, China
[d] State Key Laboratory of Continental Dynamics, Department of Geology, Northwest University, Xi'an 710069, China

ARTICLE INFO

Keywords:
Shanggong Au deposit
Pyrite
S isotope
Southern margin of the North China Craton

ABSTRACT

The Shanggong Au deposit is a world-class Au deposit in the southern margin of the North China Craton. Pyrite, as the primary Au carrier in this deposit, is an ideal mineral for dissecting the complex ore-forming process and origin of this deposit. Four types of pyrite were identified by EPMA, SEM, LA-ICP-MS, and NanoSIMS analyses: the coarse-grained cubic, disseminated pyrite (Py1) in the early ore stage (S1) and three types of the fine-grained pentagonal dodecahedron, disseminated pyrite (Py2-1, Py2-2, and Py2-3) with zoning textures in the main ore stage (S2). Py1 is relatively depleted in most metals but enriched in Co and Bi compared with other types of pyrite in S2. On the other hand, both Py2-1 and Py2-3 contain relatively high contents of As, Au, and other metals, whereas Py2-2 contains highest Au, As, Ag, Cu, Sb, Te, Tl, and Pb. Oscillatory zoning in Py2-1 resulted from repeated local fluid phase separation at the near-surface of pyrite crystal due to sharp fluid pressure fluctuation. The Au and As-rich Py2-2 was probably formed under both extrinsic fluctuations in fluid pressure and composition and intrinsic local crystal-fluid interface kinetic effects (e.g., diffusion-limited self-organization, surface electrochemistry-driven adsorption). Crystallization of Py2-1 and Py2-2 has exhausted the metals in the residual fluids, wherein the trace element-poor Py2-3 crystallized and locally replaced Py2-2 through a dissolution-reprecipitation process. Our new data and previous results suggest the ore-forming fluids were likely initial produced by degassing of the concealed pluton, and the metals were sourced from both the crust (e.g., the Taihua complex and Xiong'er Group) and the mantle. The negative $\delta^{34}S$ values for pyrite in the S2 stage might result from both the isotopic fractionation between sulfide and sulfate minerals via oxidation of the ore-forming fluid and the input of biogenic sulfur.

1. Introduction

The North China Craton (NCC) contains numerous Late Mesozoic gold (Au) deposits with a total proven reserve of 4000–5000 t (Aufarb and Santosh, 2014). These deposits mainly cluster in the eastern, southern, and northern margins of the NCC (Li et al., 2012a; Zhu et al., 2015). The southern margin is geologically defined by the Sanmenxia-Lushan Fault to the north and the Luonan-Luanchuan Fault to the south (Fig. 1b, which was affected by the orogenic event induced by the closure of the Paleo-Tethys Ocean and the subsequent Triassic collision between the Yangtze Block (YZB) and NCC (Zheng and Dai, 2018). The southern margin of the NCC and its adjacent districts in the Qinling-Dabie orogen are endowed with intensive tectonic-magmatic activities during the Late Mesozoic (Mao et al., 2010; Gao and Zhao, 2017) and large-scale Au-Mo-Ag-Pb-Zn mineralization (Mao et al., 2002, 2011; Li et al., 2012a,b; Zhao et al., 2018). This margin hosts more than 100 Au deposits that mostly cluster in the Xiong'ershan and Xiaoqinling districts and is the second-largest Au producer in China (Mao et al., 2002; Li et al., 2012a). The Au mineralization in the Xiong'ershan district is dominated by altered-rock type with minor quartz vein- and breccia-types (Chen et al., 2008; Fan et al., 2011; Tang et al., 2013). Ore-bodies are largely controlled by NE-striking brittle-ductile faults and its ore-hosting wall rocks mainly consist of volcanic rocks of the Paleo-proterozoic Xiong'er Group and metamorphic rocks of the Neoarchean-

* Corresponding author at: 511 Kehua Street, Wushan, Tianhe District, Guangzhou, GD 510640, China.
E-mail address: tpzhao@gig.ac.cn (T. Zhao).

https://doi.org/10.1016/j.oregeorev.2022.104728
Received 25 April 2021; Received in revised form 13 January 2022; Accepted 24 January 2022
Available online 29 January 2022

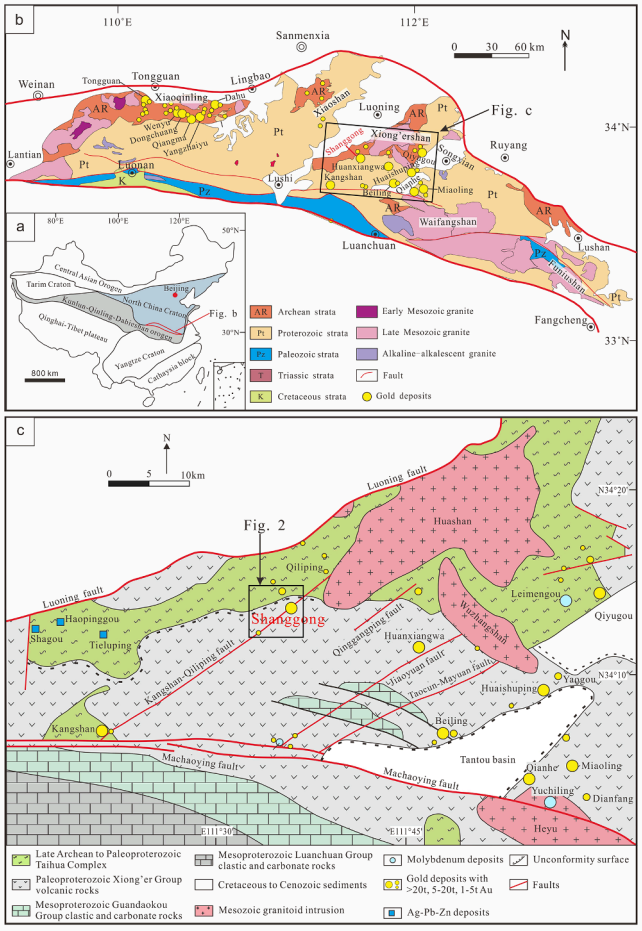

Fig. 1. (a) Major Tectonic outlines of China and (b) Geological map showing major deposits in the Xiong'er terrane, the southern margin of the North China Craton (modified after Zhao et al. 2018);

Paleoproterozoic Taihua Complex (Chen and Zhao, 1997; Fan et al., 1998; Chen et al., 2008; Huang et al., 2012).

Numerous studies of geochronology, isotopes, and fluid inclusions have been conducted for the deposits in the Xiong'ershan district, but origins of these deposits remain controversial. Previous studies attributed the ore-forming fluids to be the Yanshanian magma-derived hydrothermal fluids (Fan et al., 1994, 1998; Li et al. 2012a, Li et al., 2012b; Tang et al., 2013; Chao et al., 2020), metamorphic dehydration of the subducted slab (Chen et al., 2006, 2008; Qi et al., 2006; Tang, 2014), and devolatilization of mantle or mantle- and crustal- derived magma (Lu et al., 2003; Hu et al., 2013). Moreover, the metals were suggested to be sourced from the ancient basement or overlying strata (Fan et al., 1994, 1998; Chen et al., 2008)or devolatilization of crustal- and mantle-derived magma (Lu et al., 2003; Li et al., 2012a, 2012b; Hu et al., 2013; Tang, 2014; Tang et al., 2019). Both the Triassic collision between the NCC and YZB (Mao et al., 2002; Lu et al., 2003; Chen et al., 2006, 2008; Hu et al., 2013; Tang, 2014; Tang et al., 2019) and the lithospheric thinning of the NCC (Fan et al., 1998; Li et al., 2012a; Zhu et al., 2015) have been proposed to account for the geodynamic setting of these deposits.

The Shanggong deposit is the largest (130 t Au) and representative structure controlled altered rock-type Au deposit discovered for the first time in the Xiong'ershan district (No.1 Institute of Geological & Mineral Resource Survey of Henan, China, Report, 2019). In this study, we conducted textural and geochemical investigations on pyrite that is the foremost Au carrier in the Shanggong Au deposit. We obtained the chemical composition of different types of Au-bearing pyrite by using electron probe microanalysis (EPMA) and laser ablation-inductively coupled plasma-mass spectrometry (LA-ICP-MS). Internal textures of pyrite grains were examined by scanning electron microscope (SEM) and electron backscattered diffraction (EBSD). Furthermore, high-resolution in situ Nano-secondary ion mass-spectrometry (NanoSIMS) was utilized to acquire sulfur isotopic compositions of pyrite. Rb-Sr isochron dating of sericite closely associated with Au-bearing pyrite was used to constrain the age of mineralization. This new dataset, combined with previously reported results, allow us to comprehensively understand the ore-forming process, enrichment mechanism of Au. Additionally, this study also has great implications for regional Au metallogeny.

2. Geology setting

2.1. Regional geology

The NCC is one of the oldest continental nuclei in the world and consists of the Western and Eastern Blocks (Zhao and Cawood, 2012). Its margins were influenced by Late Paleozoic to Early Mesozoic orogenic activities (Dong et al., 1995; Zheng and Dai, 2018). After the Triassic continental collision between the NCC and the YZB and subsequent continental subduction, the southern margin of the NCC (Fig. 1b has been a part of the Qinling Orogenic Belt (QOB) (Dong et al., 1995; Wu and Zheng, 2013) and the transitional zone between the NCC and orogenic belt (Zhao et al., 2018). The Western Block of the NCC remains stable since the Paleoproterozoic and is characterized by a thick lithospheric root (>150 km) with low heat flow, weak tectonism and magmatism. Comparatively, the Eastern Block has undergone destruction, lithospheric thinning, and transformation of the tectonic regime (compression to extension) because of the westwards subduction of the paleo-Pacific plate from Late Jurassic to Early Cretaceous, accompanied by extension structures, rifted basins, voluminous mafic to felsic magmatism and Mo-Au-Pb-Zn mineralization (Mao et al., 2002; Li et al., 2012a, 2012b; Zhou et al., 2015; Zhu et al. 2011, Zhu et al., 2015; Zheng and Dai, 2018; Zheng et al., 2018; Zhao et al., 2018 and references therein).

The Xiong'ershan terrane is located in the southern margin of the NCC, immediately to the north of the QOB (Fig. 1a) and structurally bounded by the Machaoying Fault to the south and the Luoning Fault to the north (Fig. 1c) (Chen et al., 2004). Numerous secondary NNE-NE-trending faults are evenly distributed, and the Au deposits are spatially controlled by these faults in the Xiong'ershan terrane (Fig. 1c). The crust of the studied region consists of the Archean to Early Paleoproterozoic basement and overlying Late Paleoproterozoic to Phanerozoic unmetamorphosed cover sequences (Fig. 1c) (Zhao et al., 2018). The basement is dominated by Neoarchean-Paleoproterozoic Taihua Complex (2.26–2.84 Ga) that mainly consists of metamorphic rocks, such as amphibolite, felsic gneiss, migmatite, and metamorphosed supracrustal rocks (Huang et al., 2012). The Xiong'er Group formed in the period of 1.75–1.78 Ga unconformably overlays the Taihua Complex and consists mainly of intermediate to acidic lavas and pyroclastic rocks with minor intercalated sedimentary rocks (Zhao et al., 2004). Besides, the Xiong'er Group is unconformably overlain by Mesoproterozoic littoral facies terrigenous clastic rocks of the Guandaokou Group, Neoproterozoic neritic facies clastic-carbonate rocks and alkaline volcanic rocks of the Luanchuan Group (Fig. 1c). In addition, the region also accumulated lacustrine or alluvial sediments from the beginning of the Cretaceous.

The Late Mesozoic magmatism is pervasive in the southern margin of the NCC and formed mafic and felsic rocks with zircon U-Pb ages of 158–112 Ma and 148–117 Ma, respectively (Gao and Zhao, 2017). This magmatism is spatially and temporally associated with Au-Mo-Pb-Zn deposits (Mao et al., 2002; Li et al., 2012a; Zhao et al., 2018). The major granitic intrusions in the Xiong'ershan terrane and its adjacent region include the Huashan (148–127 Ma, Mao et al., 2010; Xiao et al., 2012), Wuzhangshan (156.8 ± 1.2 Ma, Mao et al., 2010), and Heyu

plutons (148–127 Ma, Guo et al., 2009; Gao et al., 2010; Mao et al., 2010). Ore-related granitic porphyry was also generally formed in this time, such as the Haopinggou (134–130 Ma, Liang et al., 2015), Shiyaogou (134 ± 1 Ma, Han et al., 2013) and Mogou (134 ± 2 Ma, Mao et al., 2010) plutons.

2.2. Geology of the Shanggong Au deposit

The Late Mesozoic Au-Mo-Pb-Zn mineralization is widely developed in the Xiong'er terrane (Zhao et al., 2018 and references therein), where numerous Au deposits are hosted in the Neoarchean high-grade metamorphic rocks and/or late Paleoproterozoic volcanic rocks (Fig. 1c). The Shanggong Au deposit, the largest Au deposit in the Xiong'er terrane, is located in the northern part of the Kangshan-Qiliping fault (Fig. 1c). This deposit contains more than 30 ore bodies that are controlled by NE-NNE-oriented faults (Fig. 1c and Fig. 2). Structural analyses suggest that these faults experienced early compressional deformation and were then reactivated by late extensional faults (Mao et al., 2006). The ore-hosting rocks in shallow levels are volcanic rocks of the Paleoproterozoic Xiong'er Group, whereas those in deep levels are metamorphic rocks of the Neoarchean-Paleoproterozoic Taihua Complex (Fig. 3). A majority of mineralized veins in this deposit strike northeast and generally dip 58°–63° NW (Fig. 3. These veins are 700 ~ 2200 m long and extend for a few hundred meters down plunge (Chen et al. 2006).

Hydrothermal alterations are common in the Shanggong deposit and mainly comprises silicification, carbonation, sericitization, and sulfidation. Three stages of mineralization and alteration in this deposit can be identified: the early ore stage (S1) with quartz-ankerite alteration, the main ore stage (S2) with Au-pyritized-phyllic alteration, and the late ore stage (S3) with quartz-calcite alteration (Fig. 4). The mineral assemblage of the S1 stage mainly comprises quartz, ankerite, and minor epidote and pyrite, and was sheared, mylonitized, or brecciated (Fig. 5a-d). The S2 is characterized by sericitization, sulfidation, and silicification (Fig. 5 and Fig. 6a-c), with two main types of ores, including breccia (Fig. 5b-d) and altered rock-type ores (Fig. 5e and f). Pyrite is the most important Au-bearing mineral (Fig. 6) and generally ingressed or

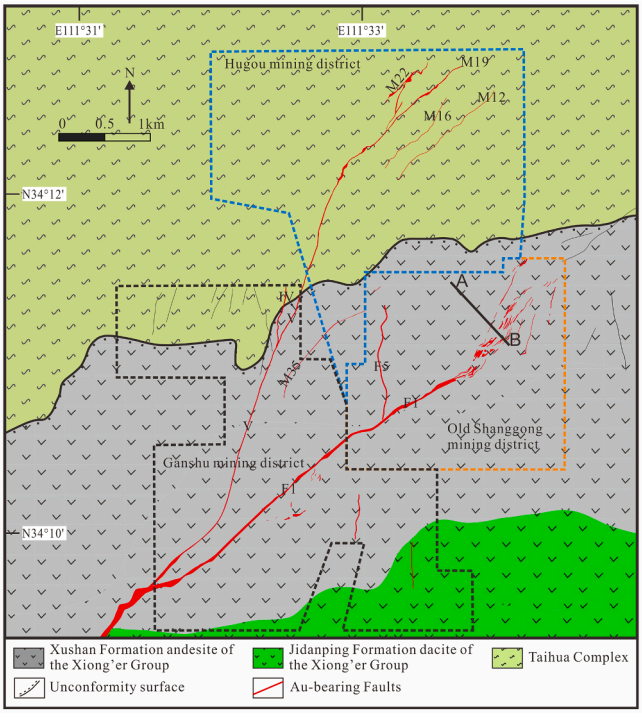

Fig. 2. Geological map of the Shanggong gold deposit (modified from the 1:10,000-scale geologic map).

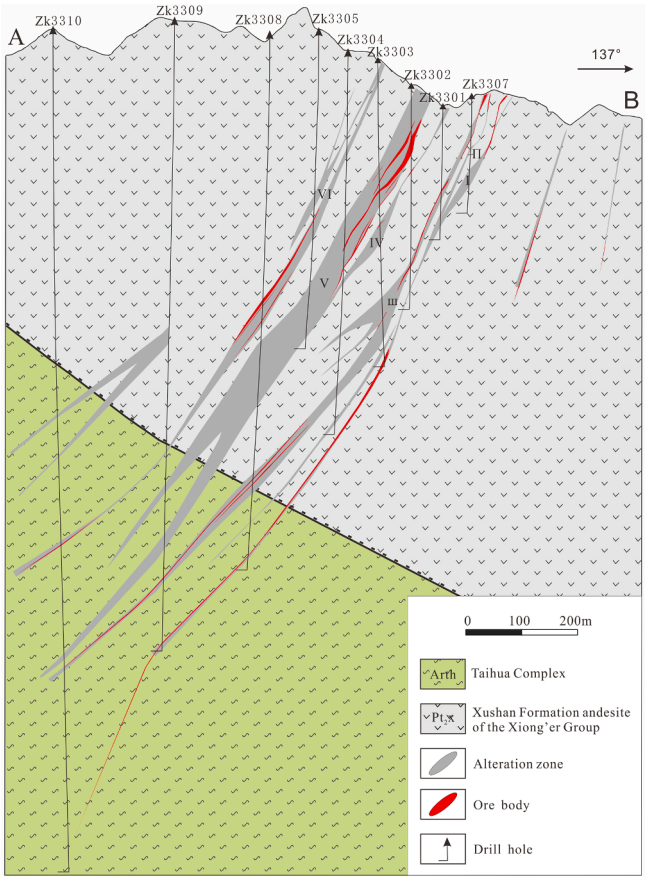

Fig. 3. Cross-section A-B in Fig. 1c.

enclosed by sphalerite, galena, and trace hessite and electrum (Fig. 6d-h). Apart from pyrite, the ores also contain minor to trace galena and sphalerite and trace chalcopyrite, magnetite, chalcocite, tetrahedrite, argentite, bornite, pyrrhotite, siderite, electrum, tellurides, and native elements (Au, Ag, etc.) (Fig. 6). Gangue minerals are mainly quartz, sericite, and chlorite, with minor epidote, ankerite, and barite (Fig. 6). The S3 is dominated by quartz-carbonate veinlets (Figs. 5f and 6c) with local chlorite, sericite, fluorite, and barite. These veinlets penetrate the mineralized fracture zones and country rocks (Fig. 5a.

3. Sampling and analytical techniques

Samples of this study were collected from the underground exploration tunnel and mainly from the orebody I_{-12} (Fig. 3) at the 706, 666, 626, and 586 levels, respectively. Polished thin sections were prepared for further analysis to investigate the mineral morphology, textures, paragenesis, and compositions.

3.1. Textural and major elements analysis

Petrographic features and textural characteristics of ores and minerals were examined by using optical microscopes, scanning electron microscopes (SEM, SUPRA 55 SAPPHIRE, ZEISS Company, Germany), and electron probe microanalysis (EPMA, JXA-8230, JEOL Company, Japan) at Guangzhou Institute of Geochemistry, Chinese Academy of Sciences.

Major element compositions of representative pyrite were determined by EPMA. The X-ray lines used for EPMA analyses: S (K_α), Fe (K_α), Co (K_α), Ni (K_α), Cu (K_α), Zn (L_α), As (L_α), Ag (L_α), Te (L_α) and Au (L_α). Operation conditions included an accelerating voltage of 20 kV and a beam current of 20 nA with wavelength dispersive X-ray spectrometers.

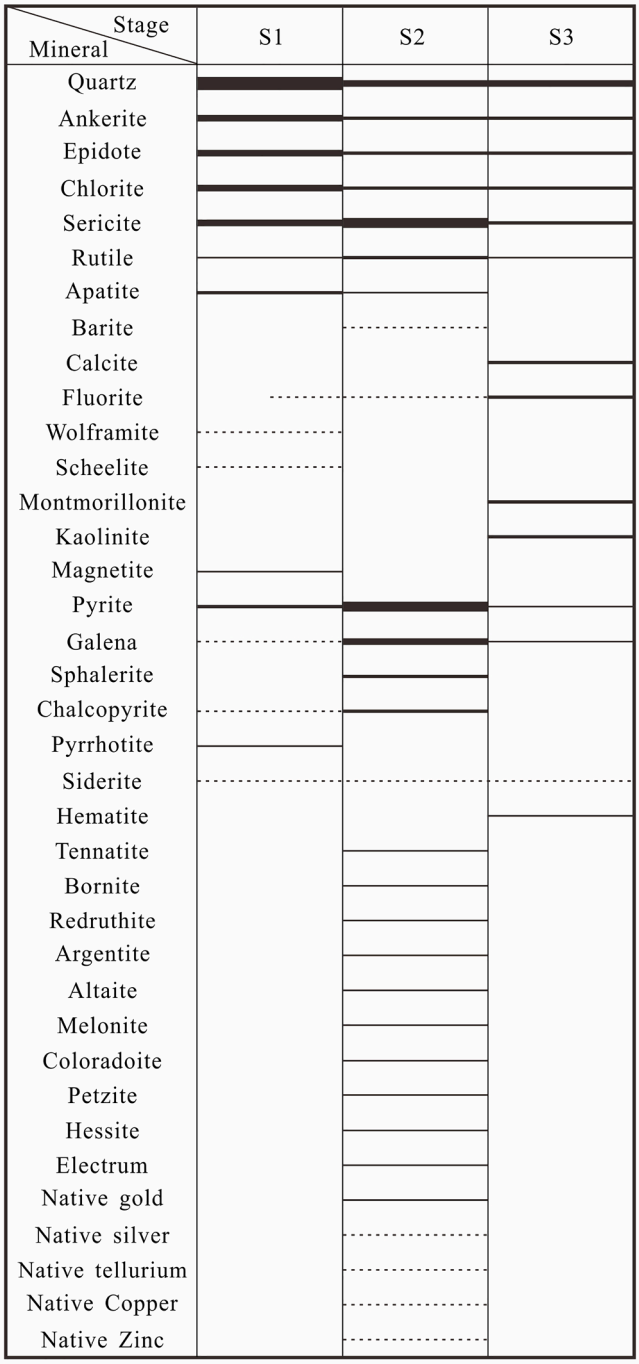

Fig. 4. Paragenetic sequence of the Shanggong gold deposit.

To improve the statistics of the count rates, peak counting times were 20 s for Fe and S, 40 s for Co, Ni, Cu, and Zn, 60 s for As, Ag, and Te, and 120 s for Au. The electron beam is ~ 1 μm in diameter. Calibration standards used were pyrite for S and Fe, sphalerite for Zn, and alloy or pure metal for Co, Ni, Cu, As, Te, Ag, and Au. The detection limits for each element were S (68 ppm), Fe (89 ppm), Co (59 ppm), Ni (53 ppm), Cu (94 ppm), Zn (136 ppm), As (115 ppm), Ag (51 ppm), Au (201 ppm), and Te (99 ppm).

Electron backscattered diffraction (EBSD) data of pyrite were collected using an Oxford HKL Nordlys II EBSD detector coupled with an FEI Quanta 450 field emission gun scanning electron microscope at the State Key Laboratory of Geological Processes and Mineral Resources in China University of Geosciences (Wuhan). The detailed analytical methods have been reported by Xu et al. (2014). The analyses were conducted with an accelerated voltage of 20 kV and a working distance of ~ 25 mm and 70 sample tilt in high vacuum mode. Besides, the orientation maps were analyzed with a step size of 1 μm.

3.2. Trace elements analysis and imaging of sulfides

Elemental mapping and trace element compositions of pyrite were performed by LA-ICP-MS at the Tuoyan in-situ Analytical Laboratory (China) using a 193 nm ArF Excimer Laser Ablation system (NWR) coupled with a thermal Fisher iCAP RQ. Spot analyses were used for individual analyses of various chemical zones known from EPMA data. Line scans were used for trace element mapping. Additionally, detailed analytical procedures for elemental mapping in pyrite have been reported in detail by Li et al. (2020). Spot ablation was performed using a 20 μm spot diameter at 5 J/cm^2 and using 10 Hz, with a 45 s baseline and 45 s ablation. Line scans were carried out using a 5 μm square spot with 20 Hz and a scan speed of 5 μm/s. Helium was used as a carrier gas to enhance the transport efficiency of the ablated material. Helium was applied as the carrier gas (0.7 L/min) and mixed with the Ar carrier gas (0.98 L/min) via a Y-connector before entering the ICP. Trace element compositions of sulfide minerals were calibrated using the NIST 610, MASS-1, and GSE-2R reference material as external standards, and iron (^{57}Fe) determined by EPMA was used as the internal standard. The standards were analyzed after every 4–10 sample analyses. The preferred values of element concentrations for reference standards are from the GeoReM database (http://georem.mpch-mainz.gwdg.de/). Off-line selection and integration of background and sample signals, time-drift correction, and quantitative calibration were performed by the software Iolite (version 4). Signals were screened visually for heterogeneities/abnormalities such as micro-inclusions or zoning. The detection limits for Co, Ni, Cu, Zn, As, Se, Ag, Sb, Te, Au, Hg, Tl, Pb, Bi were shown in the Appendix Table A3.

3.3. In situ NanoSIMS sulfur isotope analysis of pyrite

In situ S isotope analysis and elemental mapping were performed using a Camera NanoSIMS 50L at the Institute of Geology and Geophysics, Chinese Academy of Sciences, Beijing, China. The analytical procedures have been described in detail by Zhang et al. (2014). A Cs^+ beam current of ~ 7–10 pA with a diameter of 250 nm was rasterized across the sample surface for the two types of analysis. Before image and S isotope acquisitions, the selected area (25 × 25 μm^2) was sputtered with a high-intensity beam of 1nA for ~ 2 min to remove the coating and to implant enough Cs^+ into the sample surface to stabilize the yield of the secondary ions. ^{34}S and other elements were counted with electronic multipliers, whereas ^{32}S was counted by Faraday cup to avoid the quasi-simultaneous arrival effect (Yan et al. 2018). Sulfur isotopic compositions of pyrite in this study were corrected by the certified international standards of Balmat and CAR-123 pyrite and an internal reference sample of PY-1117. Images, with a pixel resolution of 256 × 256, were recorded simultaneously from the secondary ions of ^{34}S, ^{63}Cu^{32}S, ^{75}As^{32}S, ^{197}Au. Peaks were calibrated using arsenopyrite for AsS, chalcopyrite for CuS, and metallic Au.

3.4. Rb-Sr isotope analysis of ore-related sericite

To investigate the timing of alteration and mineralization, seven sericite samples from the representative ores with Quartz-sericite-pyrite alteration assemblages were dated by Rb-Sr isotope geochronology method. The ores were collected from the ore-bearing vein $V_{I\text{-}12}$, at the 706, 666, 626, and 586 levels, respectively, and they mainly consist of sericite, quartz, and pyrite.

Sericite grains for analysis were washed ultrasonically in ultrapure water and analysis-grade alcohol, before being transferred into Teflon vessels. They were spiked with ^{85}Rb-^{84}Sr spikes and dissolved in a

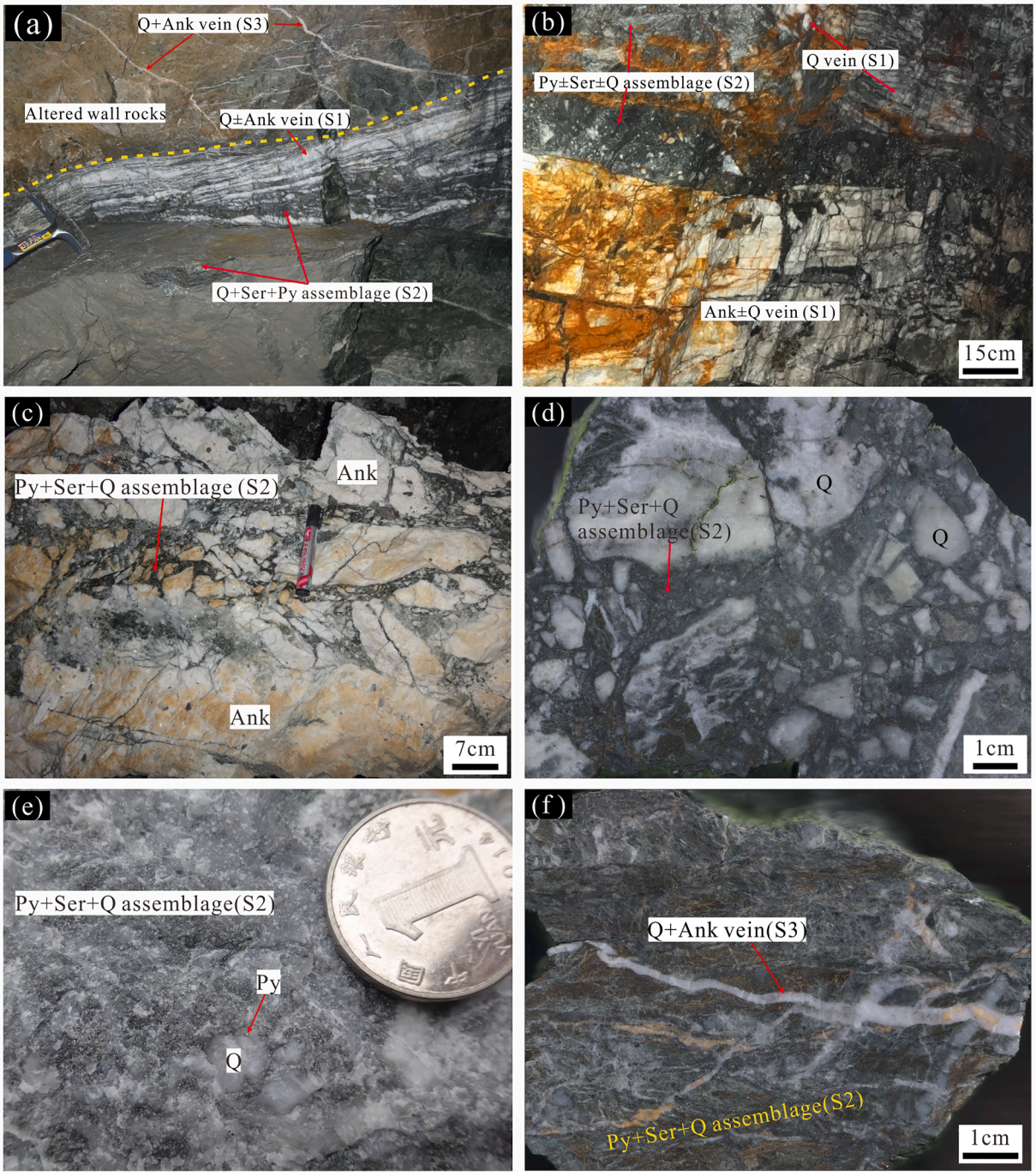

Fig. 5. (a-b) Typical orebody. The S1 quartz (ankerite) vein was intruded by quartz-sericite-pyrite vein. (c-d) Representative brecciated-type ores. The S1 quartz (ankerite) breccia is surrounded by the S2 quartz-sericite-pyrite vein. (e-f) Representative altered rock-type ores mainly consist of quartz, sericite, and pyrite. Some ores are crossed by S3 quartz + ankerite vein (f). Q-quartz, Py-pyrite, Ank-ankerite, Ser-sericite.

mixture of 3 ml ultrapure HF and 3–4 drops of ultrapure $HClO_4$. Separation and purification of Rb and Sr were conducted by cation exchange resin. The isotopic ratios of Rb and Sr were determined on a Triton thermal ionization mass spectrometer in the Isotope Geochemistry Laboratory of the Wuhan geological survey center, China Geological Survey. The $^{87}Rb/^{86}Sr$ ratios of NBS-987 show a mean value of 0.71025 ± 0.00004 (2σ). The total procedural blanks for Rb and Sr were 0.3 ng and 0.6 ng, respectively. Rb-Sr isochronal ages were calculated using the ISOPLOT software (Ludwig, 2003), using errors of 2% for $^{87}Rb/^{86}Sr$ ratios and the within-run measurement precision for $^{87}Sr/^{86}Sr$.

4. Results

4.1. Sericite Rb-Sr isochronal geochronology

Seven samples were selected for Rb-Sr isotopic dating, and the data of single sericite grains and the whole rock (17SG132A) are shown in Table 1. The samples have large ranges of Rb (334.3–505.4 ppm) and Sr (27.65–112.1 ppm) with $^{87}Rb/^{86}Sr$ ratios varying from 9.352 to 53.34. The fundamental conditions for successful isochron dating require a homogeneous initial isotopic composition for the samples and a closed isotopic system after mineral crystallization (Faure and Mensing, 2005). Samples 17SG71 deviates from the mineral Rb-Sr isochron and was

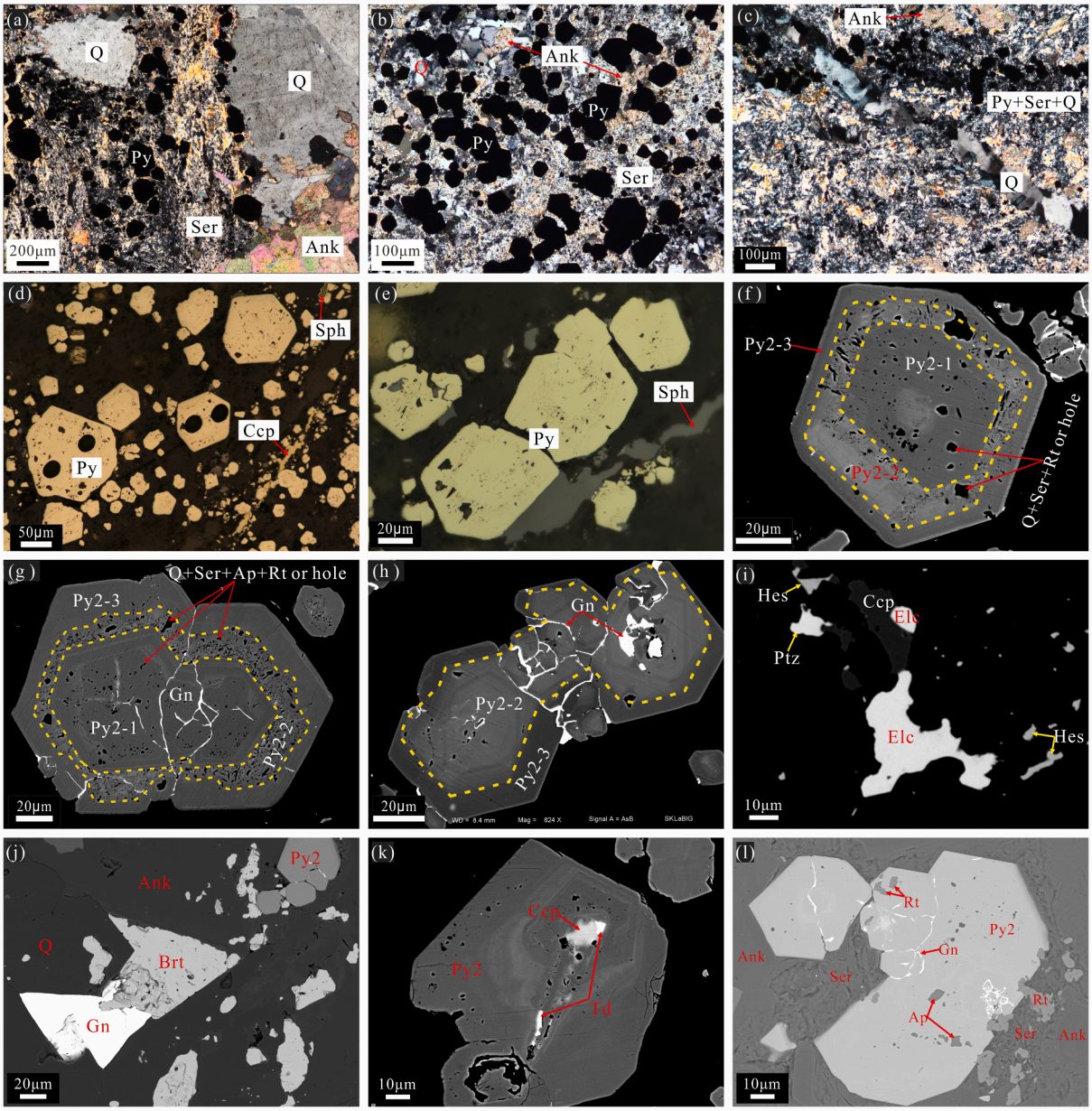

Fig. 6. Thin-section microphotographs (a-e) and backscattered electron (BSE) image (f-l) of ores. (a-c) The S2 fine-grained quartz-sulfide assemblages interspersing or cementing the S1 quartz or ankerite breccia, and cut by S3 quartz vein. (d-e) Fine-grained pyrite with zoning textures interspersed by chalcopyrite and/or sphalerite. (f-h) BSE images of the S2 pyrite. Py2-1 generally occurs as core overgrown by Py2-2. The Py2-2 is further overgrown by Py2-3. The Py2-1 contains abundant mineral inclusions and pores and was locally corroded or replaced Py2-2. In some cases, the Py2-2 zones also contain pores and inclusions of rutile, sericite, quartz, galena, but in many cases, they are absent of these inclusions or pores. Generally, Py2-3 is almost homogenous and clean. The intergranular and transgranular fractures in pyrite are usually filled by sulfides, tellurides. (i) The S2 electrum + petzite + chalcopyrite assemblages. (j) The S2 pyrite + galena + barite assemblages. (k-l) The S2 pyrite comprised chalcopyrite, tetrahedrite rutile, and apatite inclusions. Gn-galena, Sph-sphalerite, Ccp-chalcopyrite, Elc-electrum, Ptz- petzite, Hes-hessite, Td-tetrahedrite, Ap-apatite, Brt-barite, Rt-rutile.

Table 1
Rb-Sr isotope data of single-grain sericite and rocks from the Shanggong gold deposit.

Number	Sample number	Sample name	Rb (ppm)	Sr (ppm)	$^{87}Rb/^{86}Sr$	$^{87}Sr/^{86}Sr$	2σ	I_{Sr-149}
1	17SG57	Sericite	357.3	70.49	14.668	0.74376	0.00002	0.7127
2	17SG71	Sericite	337.8	37.05	26.538	0.80696	0.00003	0.7507
3	17SG66	Sericite	386.3	37.43	29.953	0.77717	0.00006	0.7137
4	17SG77	Sericite	334.3	100.50	9.6157	0.73468	0.00002	0.7143
5	17SG81	Sericite	405.6	49.88	23.574	0.76337	0.00007	0.7134
6	17SG132	Sericite	505.4	27.65	53.337	0.82914	0.00002	0.7162
7	17SG132A	Whole rock	362.5	112.1	9.3520	0.73817	0.00002	0.7184

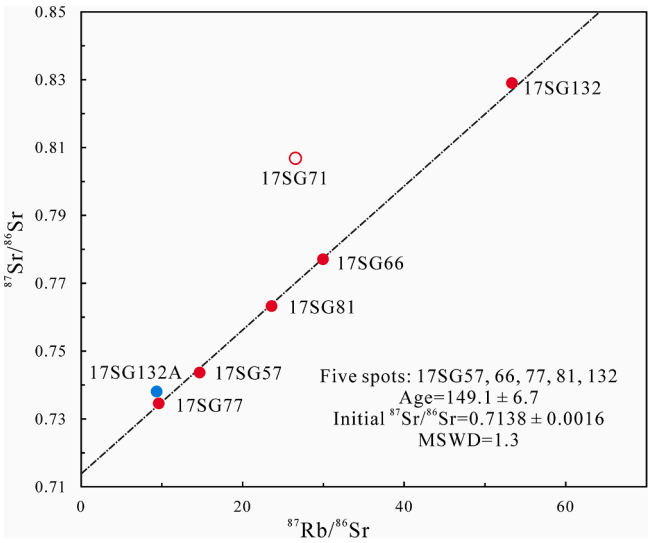

Fig. 7. Sericite Rb-Sr isochron ages for the Shanggong deposit.

hence excluded for isochronal age calculation (Fig. 7). The remaining five analyses yield a good isochron age of 149.1 ± 6.7 Ma, with an initial $^{87}Sr/^{86}Sr$ ratio of 0.7138 ± 0.0016 (MSWD = 1.3).

4.2. Textures and compositions of pyrite

Based on the petrographic observations, SEM and EPMA analyses in this study and previous studies (Fan et al., 1998; Chen et al., 2006; Tang et al., 2019), two major generations of pyrite were identified in the Shanggong Au deposit. The detailed compositions of these pyrites are shown in Appendix Table A2.

The S1 pyrite (Py1) generally occurs as coarse-grained cubic grains disseminated in the quartz ± pyrite veins and adjacent altered rock (Chen et al., 2006; Tang et al., 2019). The Py1 grains have average S of 52.14 ± 0.43 wt% and Fe of 45.97 ± 0.33 wt%, respectively, and have Au contents generally below the EPMA detection limit (Li et al., 2004).

Pyrite in the S2 stage is characterized by disseminated, fine-grained pentagonal dodecahedron grains (Fig. 6a-f), which are commonly composed of three different zones, named as Py2-1, Py2-2, and Py2-3 from inner outward (Fig. 6f-h). Py2-1 generally presents as a core containing mineral inclusions and pores rimmed or locally corroded or replaced by Py2-2 (Fig. 6f-g). The BSE images of some Py2-1 grains show oscillatory zones (Fig. 6g) represented the rhythmic alternation of dark bands with low As (below the detection limit (b.d.L) to 0.30 wt%) but high S (51.57 ~ 53.65 wt%) and bright bands with high As (1.47 ~ 4.81 wt%) but low S (47.69 ~ 51.10 wt%). The average compositions of Fe in the dark and bright bands are 46.62 ± 0.36 wt% and 45.55 ± 0.0.48 wt %, respectively. The Au contents in the two bands are mostly near or below the EPMA detection limit.

Py2-2 is usually a bright band of As- and Au-rich overgrowth on Py2-1 with 1–20 μm in width and further rimed by Py2-3 (Fig. 6f-g). However, some Py2-2 can also be present as a core directly surrounded by Py2-3 (Fig. 6h). Most Py2-2 are free of pores or mineral inclusions (Fig. 6h) with only minor containing pores and inclusions of sphalerite, galena, and silicate minerals such as rutile, sericite, quartz, and apatite (Fig. 6f-g), suggesting the complete recrystallization of Py2-2 and/or the sealing of the porosity. The Py2-2 grains have S and Fe average value at 49.83 ± 0.83 wt% and 44.93 ± 0.48 wt%, respectively, and the Au contents have an average content of 0.32 ± 0.11 wt%.

Py2-3 generally occurs as a subhedral to euhedral rim on Py2-2 and is almost homogenous and free of any mineral inclusions or pores (Fig. 6f-h). The contacts between Py2-2 and Py2-3 are sharp, and the reaction fronts are planar and/or curvilinear, suggesting that Py2-2 was replaced by the Py2-3. The Py2-3 grains have average S of 53.07 ± 0.37 wt% and Fe of 46.35 ± 0.30 wt% with low concentrations of As (0.01 ~ 0.08 wt %). The corresponding Au contents are often below the EPMA detection limit.

4.3. Trace element compositions and mapping of pyrite

To investigate the evolution of ore fluid and Au mineralization in the Shanggong deposit, we carried out detailed LA-ICP-MS trace element analyses on the S2 pyrite with complex textures, including 20 analyses on Py2-1, 11 on Py2-2, and 13 on Py2-3 (Appendix Table A3). The results, combined with the S1 pyrite (Py1) data reported by Tang et al. (2019), are summarized in Table 2 and shown in Fig. 8.

4.3.1. Pyrite in S1 stage

The coarse-grained, euhedral, cubic Py1, compared with the S2 pyrites, is relatively depleted in As, Au, Ag, Ni, Cu, Sb, and Pb, but enriched in Co and Bi (Fig. 8). The Au contents in Py1 vary from 0.65 to 70 ppm, while As contents vary from 0.12 to 8.50 ppm (Table 2). The large ranges of Au, Ag, Cu, and Pb in Py1 are probably related to the occurrence of micro-inclusions with these elements (Tang et al., 2019).

4.3.2. Pyrite in S2 stage

The subhedral to euhedral Py2-1 has much higher contents of As, Ag, Ni, Cu, Sb, and Pb compared with Py1 (Fig. 8). The Au contents of Py2-1 vary from below detection limit (b.d.L.) to 29 ppm, whereas As contents range from 176 to 5348 ppm (Table 2). LA-ICP-MS mapping results show that Py2-1 is locally enriched in most trace elements (Fig. 9), which might result from the overprints of ore fluids that precipitated Py2-2.

In contrast to other types of pyrite, Py2-2 is enriched in As (range = 18644 ~ 55327 ppm) and Au (range = 1433 ~ 4511 ppm) (Figs. 8 and 9; Table 2). Py2-2 also contains elevated elements of Ag, Cu, Sb, and Tl (Figs. 8 and 9; Table 2). Besides, LA-ICP-MS mapping results show Au are closely associated with As, Ag, Cu Sb, Te, and Tl (Fig. 9.

The clean Py2-3 has lower trace element compositions compared with Py2-2 (Fig. 8), such as As, Au, Ag, Cu, Sb, Tl, and Pb (Fig. 8; Table 2). Most analytical data of Zn, Sb, Hg, and Bi in Py2-3 are below the detection limit (Appendix Table A3. LA-ICP-MS spot analyses and mapping results show Py2-1 and Py2-3 have similar trace element contents (Figs. 8 and 9).

The smooth LA-ICP-MS time-resolved spectra with only minor and weak spikes of most trace elements in typical Py2-1, Py2-2, and Py2-3 (Fig. 10) indicate these metals occur mainly as solid solutions and partially as nanoparticles. This is consisted with our previous results (Meng et al., 2021). Spikes of the Pb, Cu, Te, Ag, Au, and time-resolved spectra suggest a possibility of the occurrences of galena, chalcopyrite, hessite, electrum, and free silver (Fig. 10), respectively.

4.4. Sulfur isotope compositions of pyrite

In this study, systematic sulfur isotope analyses of pyrite formed in the S2 stage were carried out using NanoSIMS. The sulfur isotopic compositions of these pyrites, including 47, 31, and 17 spot analyses for Py2-1, Py2-2, and Py2-3, respectively, are graphically shown in Fig. 11, and the detailed data are provided in Appendix Table A4-1. Py2-1, Py2-2, and Py2-3 are characterized by negative $\delta^{34}S$ values with ranges of −16.9 ~ −3.3‰ (average of −11.0‰), −13.1 ~ −7.0‰ (average of −10.7‰), and −13.9 ~ −6.2‰ (average of −11.0‰), respectively. However, Py1 is evidently more enriched in $\delta^{34}S$ (−2.7 ~ 7.2‰, average of 3.7‰, Tang et al., 2019) than that of the S2 pyrites.

5. Discussion

5.1. Age of the Shanggong Au deposit

Sericite grains for Rb-Sr isotopic dating were extracted from the

Table 2
Trace elemental concentrations (ppm) of pyrite from the Shanggong Au deposit in the Xiong'ershan district, the Southern margin of the North China Craton.

Type	Co	Ni	Cu	Zn	As	Se	Ag	Sb	Te	Au	Tl	Pb	Co/Ni
Py1 (n = 18)													
Avg.	335	9.83	130	31	1.30	8.39	1.11	0.19	478	11.6	nd	10.8	106
Min.	1.04	0.10	0	0	0.12	0.56	0.011	0	18	0.65	nd	0	0.79
Max.	1050	72	1940	480	8.50	39.9	10.2	1.41	3930	70.0	nd	143	524
Py2-1 (n = 20)													
Avg.	115	187	53.3	36.7	1547	bdl	7.41	12.7	8.44	11.1	0.63	100	0.59
Min.	20.3	65.1	5.97	2.37	176	bdl	0.075	2.03	0.32	0.06	0.03	2.83	0.20
Max.	593	440	385	187	5348	bdl	29.5	34.4	18.9	29.2	3.10	526	1.35
Py2-2 (n = 11)													
Avg.	101	153	1765	14.2	36,086	5.96	356	59.6	372	3108	9.32	214	0.73
Min.	2.13	38.2	354	4.48	18,644	1.27	148	24.8	115	1433	2.76	83.2	0.08
Max.	298	362	3176	33.8	55,327	11.0	1152	109	812	4511	21.7	415	1.32
Py2-3 (n = 13)													
Avg.	64	90.4	250	10.69	335	5.18	6.08	6.63	7.84	6.64	0.49	27.5	0.86
Min.	1.20	14.1	18.8	10.69	3.94	0.55	0.20	4.38	0.91	0.13	0.046	0.86	0.29
Max.	205	323	1086	10.69	2018	16.7	22.7	10.7	32.3	31.5	1.86	103	1.52

Note: (1) bdl denotes below detection limit; (2) n.d. denotes no data; (3) The whole dataset is listed in Appendix Table A3.

altered rock-type ores from the Shanggong Au deposit. Petrographic observations reveal that sericite is closely associated with Au-bearing pyrite in the ores (Fig. 6a-c) and occurs as inclusions in pyrite (Fig. 6f-g), suggesting that the two minerals have formed from a common hydrothermal activity. The whole-rock sample of 17SG132A plots close to the mineral isochron (Fig. 7), suggesting that the Rb-Sr isotopic compositions have reached equilibrium among minerals in the sample. Furthermore, the Rb-Sr isochronal age of sericite has a small error and low MSWD value (1.3, Fig. 7), indicating that the age of 149.1 ± 6.7 Ma is reliable (Li et al., 2008) and can represent the timing of the Au mineralization in the Shanggong deposit. This age is broadly similar to those of the adjacent Shagou Ag-Pb-Zn deposit (147 ~ 145 Ma, Mao et al., 2006) and other Late Jurassic-Early Cretaceous Au deposits in the southern margin of the NCC (Appendix Table A1), such as the Xiaoshan (156 ± 6.7 Ma, Tang, 2014), Dongtongyu (143 ± 1.4 Ma, Li et al., 2012a, b), Luzhoukou deposit (154 ± 1.1 Ma, Li et al., 2012a). This age is also consistent with those of widespread Mo deposits were also widely developed, such as the Shijiawa (142 Ma), Balipo (155 Ma), Yechangping (145 Ma), Nannihu-Sandaozhuang (144 Ma), Shangfanggou (144 Ma), Huoshenmiao (147 Ma), and Dawangou (146 Ma) deposits (Zhao et al., 2018 and references therein). Additionally, felsic magmatism was extensive during this period (Zhao et al., 2018). These consistent chronological data suggest the Rb-Sr isochron age of this study is convincing.

Previous Rb-Sr isochron ages constrained the Au mineralization of Shanggong deposit at 242 ± 11 Ma, 165 ± 7 Ma, and 113 ± 6 Ma (Zhang et al., 1994), corresponding to the early, middle, and late stages of mineralization (Chen et al., 2006; Chen et al., 2008), respectively. $^{40}Ar/^{39}Ar$ plateau ages of sericite (227.7 ± 1.4 Ma, 236.5 ± 2.5 Ma; Tang, 2014) suggest a Triassic hydrothermal event in this deposit, which predated the regional Au mineralization peak ages of 132–125 Ma (Zhao et al. 2018). However, the $^{40}Ar/^{39}Ar$ plateau ages of minerals would be older than their formation ages due to the ^{39}Ar recoil losses during irradiation, especially for minerals with fine-grained and/or low crystallinity (Dong et al., 1995). Collectively, we proposed the main Au mineralization should be constrained at Late Jurassic-Early Cretaceous but cannot preclude the possibility of a Triassic hydrothermal activity in the Shanggong deposit.

5.2. Genesis of pyrite and ore-forming fluid evolution

Pyite1 is disseminated in the coarse-grained quartz ± pyrite veins and the adjacent altered rocks, especially at their boundaries (Fan et al., 1998; Tang et al., 2019). Py1 is relatively depleted in Au, Ag, Ni, Cu, Sb, and Pb compared to the S2 pyrites (Fig. 8). These suggest that the Py1 could have resulted from the interactions between wall-rock and initial ore-forming fluids with low contents of trace elements and have precipitated from a condition with high fluid-rock ratios.

The oscillatory zoned S2 pyrite was formed contemporaneously with pyrite-sericite-quartz alteration (Fig. 6a-c), including Py2-1, Py2-2, and Py2-3 (Fig. 6f-h). Py2-1 generally occurs in the core of pyrite grains and is rimmed by Py2-2, which is further rimmed by Py2-3. Pyrite with well-developed zonation has been widely reported in previous studies (Baker et al., 2009; Deditius et al., 2009; Peterson and Mavrogenes, 2014; Velasquez et al., 2014; Wu et al., 2019). Changing conditions of ore-forming fluids such as temperatures, pressures, and compositions have been proposed to account for the compositional zones in pyrite (Baker et al., 2009; Deditius et al.., 2009; Peterson and Mavrogenes, 2014; Fougerouse et al., 2016a; Wu et al., 2019).

Changes in fluid compositions of multiple hydrothermal events usually result in different stages of sulfides with distinct sulfur isotopic compositions, irregular boundaries, and/or corrosion textures between the alternating bands (Barker et al. 2009; Peterson and Mavrogenes 2014; Fougerouse et al., 2016a). In this study, Py2-1 contains some concentric oscillatory zones, and Py2-2 is parallel to the crystal growing surface (Figs. 3e-h and 5f-g). The contacts between Py2-2 and Py2-3 are sharp, and the reaction fronts are planar and/or curvilinear, suggesting Py2-3 precipitated continuously from fluid after Py2-2 and limitedly replaced the Py2-2 (Figs. 6f-h and 11b). In terms of isotopic compositions, the $\delta^{34}S$ values of Py2-1, Py2-2, and Py2-3 are very similar (Fig. 11a) with only a small $\delta^{34}S$ variation from the core to the rim in a single pyrite crystal (Fig. 11c), suggesting the three types of pyrite have precipitated from a common fluid. The Euler orientation image of the selected pyrite grain (SG44-5) confirms that Py2-1, Py2-2, and Py2-3 have the same crystallographic orientation (Fig. 12b). The EBSD map shows slight crystallographic misorientations of the selected pyrite zones (Fig. 12c), which can be interpreted as low-angle subgrain boundaries trigged by intragranular plastic deformation (Li et al., 2016). Collectively, these data suggest that Py2-1, Py2-2, and Py2-3 probably have formed from the same hydrothermal event rather than multiple hydrothermal events.

Varying compositions of a single hydrothermal fluid driven by the pressure fluctuation in fluids have been proposed to interpret the formation of oscillatory zoning in pyrite (Velasquez et al. 2014; Baker et al., 2009; Peterson and Mavrogenes, 2014; Wu et al., 2018, 2019). The S2 pyrites of the Shanggong deposit are generally hosted in structurally controlled breccia and altered rock-type ores (Fig. 5d- f) and show sharp transition among the micron-scale compositional zones of Py2-1, Py2-2, and Py2-3 (Fig. 6f-h). These observations are indicative of fluctuations in bulk fluid conditions. Au mineralization in this study is closely

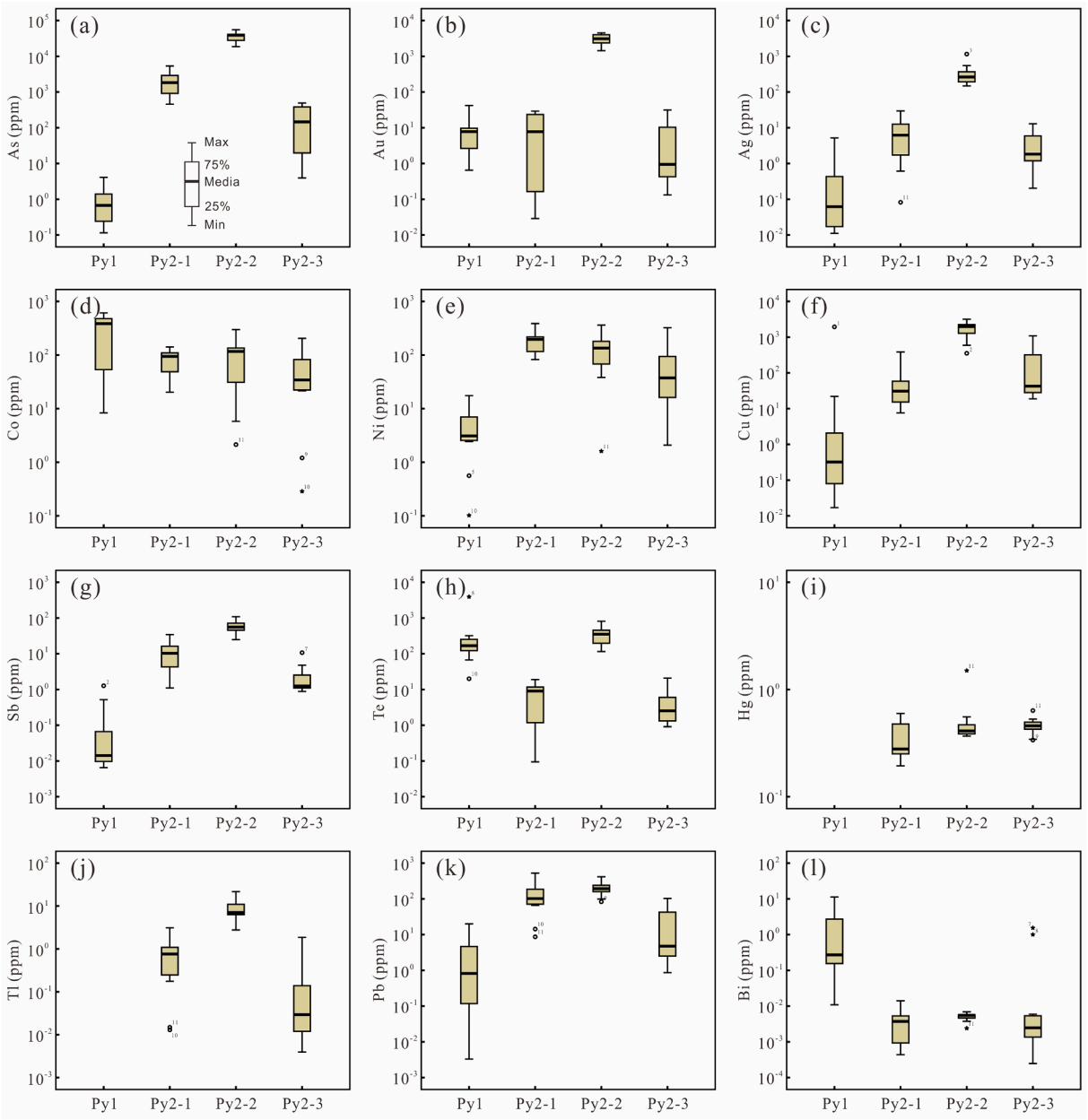

Fig. 8. Box plots of trace element compositions of Py1, Py2-1, Py2-2, and Py2-3 from the Shanggong deposit. Note: (1) The whole dataset is listed in Appendix Table A3. (2) Py1 lacks data of the Hg and Tl contents.

constrained in faults and its altered wall-rock (Fig. 3). The ore-forming fluid pressure would increase with continuous shear strain and fluid replenishment until it exceeds the lithostatic pressure, then starts the shear failure and produces the hydraulic extensional fractures around the early formed Py2-1 grains (Peterson and Mavrogenes, 2014; Cox, 2016; Li et al., 2018). This would trigger the rapid drop in fluid pressure, which was followed by ore fluid phase separation. Previous fluid inclusion studies have confirmed the occurrence of fluid phase separation in the Shanggong deposit (Fan et al., 1998; Chen et al., 2006). Recent studies have suggested incompatible trace elements such as Au, As, Ag, Cu, Sb, Te, and Tl, prefer partitioning into the liquid phase relative to the vapor phase under moderate temperatures (<400 °C) (Kouzmanov and Pokrovski, 2012, and references therein). Thus, phase separation caused by the repaid fluid pressure fluctuations would increase the concentrations of dissolved As, Au, and other metals in the liquid phase and even oversaturate the liquid to further produce the As-rich bright zones in Py2-1 (Fig. 13b). Continued As-rich pyrite growth would deplete the incompatible trace elements-rich fluid in the newly formed pyrite-fluid interfaces. Furthermore, combined with the replenishment of bulk fluid in the interface, these processes would drive the fluid system back to the beginning again. Consequently, the As-poor dark bands in Py2-1 were formed under these conditions (Fig. 13c). Successive shearing deformation and fluid replenishment would restart the above cycle to produce alternating zones in Py2-1 (Fig. 13d). Thus, we propose that fluid pressure fluctuations induced by successive shearing deformation should be responsible for the formation of the oscillatory-zoned Py2-1 pyrite. Besides, the chemistry of dark bands with low concentrations of As and Au in Py2-1 could approximately represent the initial signature of the Py2-1 hydrothermal fluids, whereas those of the bright bands are indicative of the evolved fluid that experienced phase separation.

Generally, the boundaries between the clean Py2-3 and the complex Py2-2 are sharp and vary from planar to curvilinear in the same grain, excluding the simple Py2-3 overgrowth on Py2-2. These textures suggest a limited fluid-mediated pseudomorphic dissolution-re-precipitation

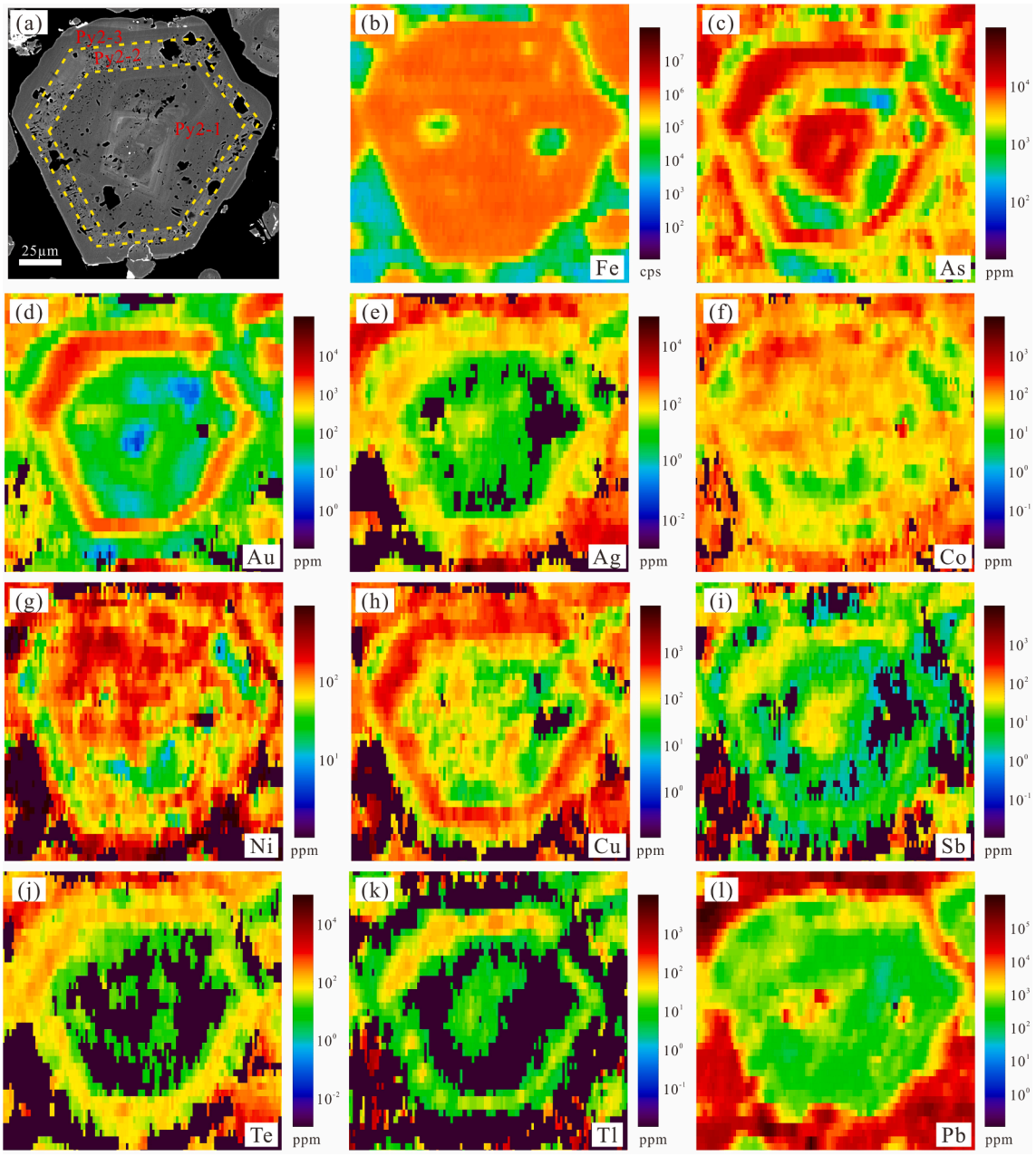

Fig. 9. LA-ICP-MS trace element maps of aggregates of Py2-1, Py2-2, and Py2-3 from the Shanggong deposit.

process (Fougerouse et al., 2016a). The lower Au and other trace elements of Py2-3 compared with Py2-2 (Fig. 8) imply the fluid that precipitated Py2-3 is poor in these elements. The residual fluid phase would become depleted in Au and other trace elements because of the precipitation of large amounts of Py2-1 and Py2-2. Then, this fluid was transported to the Py2-2-fluid interface and subsequently produced trace elements-poor Py2-3, and limitedly replaced Py2-2 by a dissolution-reprecipitation process (Fig. 13f). Moreover, this replacement might release minor Au and other elements from Py2-2 into the hydrothermal fluid and reprecipitate as nanoparticles in the same pyrite crystal (Fig. 10c) and/or its adjacent (Fig. 6)i. Besides, the presence of tellurides (e.g., hessite, electrum) and sulfides (e.g., sphalerite, galena) in the microcracks and intergranular fractures of pyrite (Figs. 6g-h and 13g) suggest the tellurium fugacity increased significantly with dramatic decreases of $\log f S_2$(g) and pH, and the logical Au oversaturation in the remained hydrothermal fluids. These might be triggered by the precipitation of large amounts of Py2-1, Py2-2, and Py2-3, and input of the new Te-rich hydrothermal fluid (Zhang and Spay, 1994).

5.3. Enrichment mechanisms of Au and As in Py2-2 pyrite

As discussed above, Py2-2 generally has a sharp boundary with Py2-1 and is parallel with its growing crystal surface (Fig. 6f-h), suggesting that Py2-2 directly precipitated from the ore fluids and overgrew on Py2-1. Au and As, Ag, Cu Sb, Te, and Tl are significantly enriched in Py2-2, implying that the hydrothermal fluid precipitated Py2-2 carried high budgets of these elements. The fluid might result from multiple stages of phase separation of the initial ore-forming fluid and a new pulse of trace elements-rich fluid. Notably, Py2-2 contains up to ~ 4511 ppm Au and 55327 ppm As (Table 2), which is consistent with arsenian pyrite with high contents of Au and As (Deditius et al., 2014 and reference therein). However, the concentrations of Au and As in metallogenic hydrothermal fluids are generally very low (1–100 ppb Au and 0.10–100 ppm As; Mikucki, 1998; James-Smith et al., 2010; Aufarb and Groves, 2015).

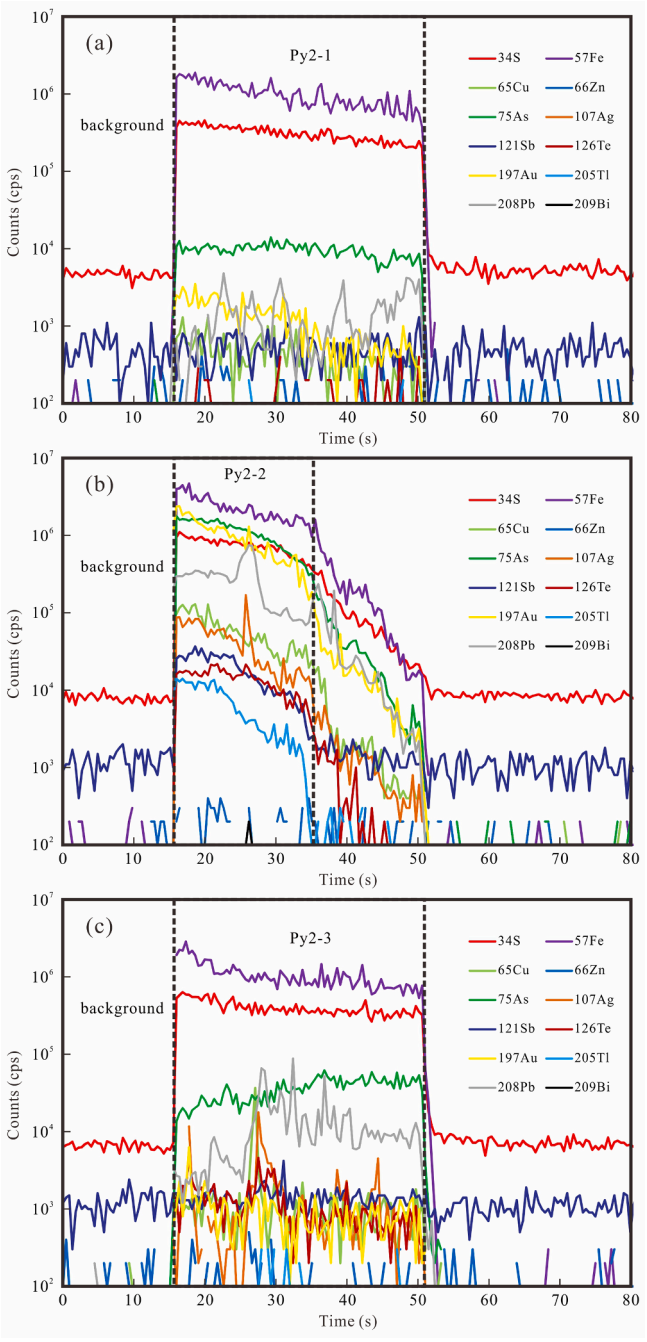

Fig. 10. Representative LA-ICP-MS time-resolved depth profiles of Py2-1, Py2-2, and Py2-3 from the Shanggong deposit.

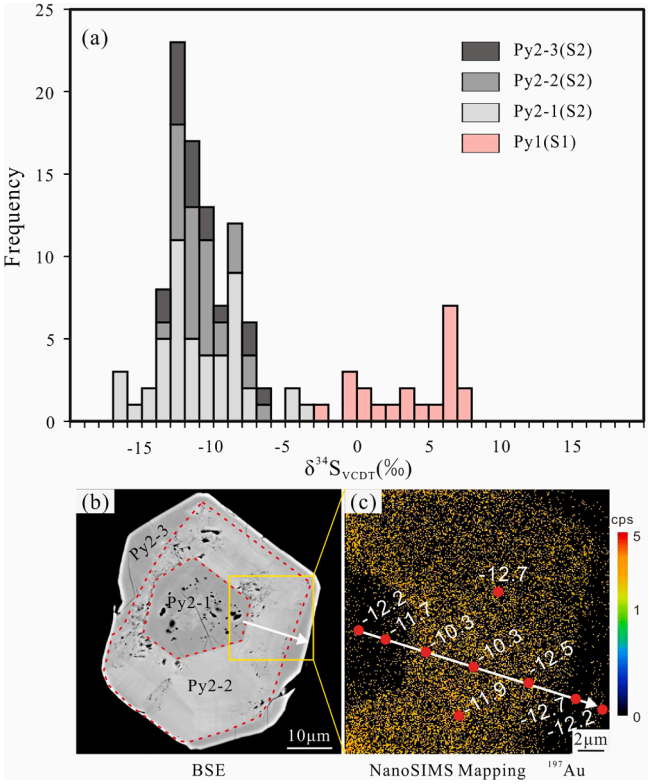

Fig. 11. (a) Histogram of the sulfur isotopic compositions of the Py1, Py2-1, Py2-2, and Py2-3 from the Shanggong deposit. (b) BSE image of pyrite. (c) Variation of $\delta^{34}S$ values of zoned pyrite, including Py2-1, Py2-2, and Py2-3. Note: (1) The whole dataset is listed in Appendix Table A4-1.

This contradictory relation suggests that Au-As-rich zones in pyrite are less likely to have directly precipitated from their patent ore-forming fluids.

Many studies have emphasized that cyclical fluid flows or multistage hydrothermal fluid processes are beneficial to form and refine Au deposits (Peterson and Mavrogenes, 2014; Fougerouse et al., 2016a; Xing et al., 2019). These cyclical processes would produce a high fluid-rock ratio, which is largely responsible for the formation of Au and As-zones in pyrite (Mikucki, 1998; Meffre et al., 2016; Xing et al., 2019). The extensive hydrothermal alterations in the ore-hosting faults (Fig. 6a-c) suggest the high fluid-rock ratios in mineralization systems in the Shanggong deposit. This would promote Au accumulation in pyrite.

Furthermore, near-surface kinetic dynamics (such as diffusion-limited self-organization) can also play an important role in the enrichment of trace elements in minerals (Watson, 2004; Fougerouse et al., 2016b; Wu et al., 2019 and references therein). Previous numerical modeling studies suggested that different self-organized nonlinear feedback processes on the fluid-mineral interface can produce centimeter- to submicron-scale chemical zoning (Putnis et al., 1992, Putnis, 2002; Wang et al., 2009). The diffusion-limited self-organization model has been used to interpret the formation of zones in calcite (Watson, 2004) and pyrite (Wu et al., 2019). According to this model, during the growth of a continuous crystal layer, when the crystal growth rate was faster than the diffusion fate of incompatible elements in the near-surface fluid layer, these elements would become enriched at the crystal-fluid interface. Consequently, the new-formed crystal layer in contact with the near-surface fluid layer would efficiently incorporate these elements and forming the incompatible elements-rich zones in the crystal (Watson, 2004; Wu et al., 2019 and references therein). However, continued crystal growth would consume the fluid incompatible elements and essential contents (Fe and S) in the fluid-crystal interface, resulting in a decrease in crystal growth rate (Wu et al., 2019) and the subsequent new-formed layer with relatively low incompatible elements. Replenishment of ore-forming fluid into the interface would restart the above cyclic process to produce oscillating zones with trace element depletion and/or enrichment. Besides, when a sufficient amount of ore-forming materials were transported to the crystal-fluid interface, a continuous compositional zone with a relatively larger width could be formed via a diffusion-limited organization process. Py2-2 can contain some silicate mineral inclusions and continuous zones (Fig. 6h), suggesting that it had a rapid growth rate and was formed with fluctuations in fluid conditions. In the Shanggong deposit, the ion diffusion rate should be slower relative to the pyrite crystallization rate because the temperature of ore-forming fluids of the main ore stage was relatively low (300-220 °C, Chen et al., 2006). Thus, we propose the pyrite crystal growth rate was faster than the near-interface diffusion

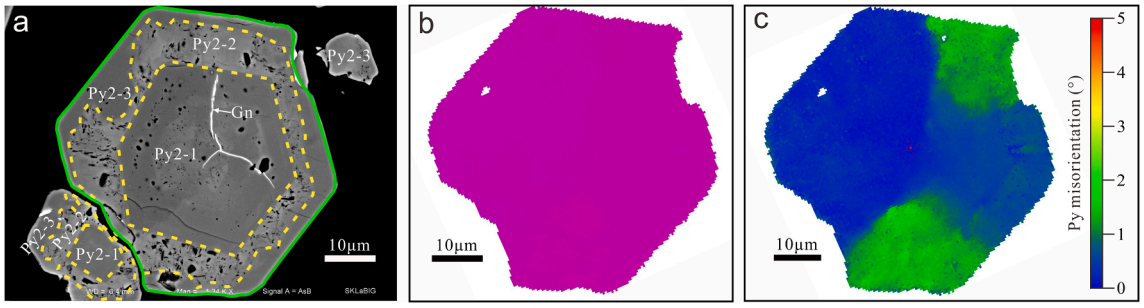

Fig. 12. Results of EBSD analysis of selected pyrite grains in S2. (a) BSE image of pyrite. Py2-2 is coated by Py2-3 and overgrows porous Py2-1. (b) Euler orientation image showing the aggregate is composed of a single pyrite grain with the same color. (c) Colored EBSD image showing slight crystallographic misorientations (0°–5°) in the selected pyrite grain.

rate of trace elements, facilitating the enrichment of fluid incompatible elements such as Au, As, Ag, Cu Sb, Te, and Tl in Py2-2 (Watson, 2004; Wu et al., 2019). Additionally, on the semi-conduction As-bearing Py2-2 surface, the surface electrochemistry-driven adsorption of Au and its associated element-bearing complexes would cause the accumulation of these elements at the pyrite-fluid interface (Mikucki, 1998 and references therein). Combined with the diffusion-limited self-organization, this process would also promote the incorporation of these elements in the new-formed Py2-2. Moreover, thermodynamic calculations demonstrated that rapid decompression and its induced phase separation in the fluid would also decrease the temperature under adiabatic conditions and further facilitate As and Au enrichment in pyrite (Pokrovski et al., 2002; Perfetti et al., 2008; Kouzmanov and Pokrovski 2012). Collectively, we propose that the significant enrichment of Au and other metals in Py2-2 could have resulted from both extrinsic (e.g., fluctuations in fluid pressure and composition) and intrinsic processes such as local crystal-fluid interface kinetic effects (e.g., diffusion-limited self-organization, surface electrochemistry-driven adsorption) (Fig. 13e).

5.4. A possible magmatic affinity

The sulfur isotopic composition of pyrite is strongly controlled by the fO_2, pH, T, and isotopic composition of hydrothermal fluids (Ohmoto, 1972). Under the low fO_2 and pH conditions, the $\delta^{34}S$ values of sulfide minerals precipitating from the ore-forming fluids are approximately equal to the $\delta^{34}S_{\sum S}$ value of the solutions (Ohmoto, 1972). The intergrowth of pyrite and pyrrhotite indicates reduced conditions of the ore-forming fluids in the S1 stage. Besides, the fluid also has a low pH value (4.7 ~ 7.7 with an average of 5.6, Chen et al., 2006), implying that the $\delta^{34}S_{\sum S}$ values of the fluid were approximately equal to that of pyrite (Py1) in the S1 stage (−2.7 ~ 7.2‰, Tang et al., 2019). Notably, the $\delta^{34}S$ values of Py1 are consistent with those of typical magmatic-hydrothermal deposits (−5 ~ 5‰, Ohmoto and Rye, 1997; Hoefs, 2009), the Taihua Complex (1.3 ~ 5.7‰, Table A4-2), Xiong'er Group (1.3 ~ 5.7‰, Table A4-2), and mantle (−3 ~ 3‰, Chaussidon and Lorand, 1990). Therefore, the S1 stage sulfur is most likely from a magmatic source and partially derived from the mantle and the surrounding rocks.

The $\delta^{34}S$ values of the S2 stage pyrites are much more negative than those of Py1 (Fig. 11a). Generally, the negative $\delta^{34}S$ values reflect either a source with an anoxic environment or isotopic fractionation during the evolution of the mineralizing fluids. The paragenesis of barite and apatite (Fig. 6j) indicates the relative oxidized condition of the ore-forming fluid in the S2 stage (Tang et al., 2013). During this stage, both the large input of meteoric water proved by Fan et a. (1994) and the fluid pressure fluctuations (Hodkiewicz et al., 2009; Wu et al., 2019) evidenced by brecciation (Fig. 5b-d), oscillatory zones (Fig. 6g-h) and fluctuations in physicochemical parameters of fluid inclusions (Fan et a., 1994, Chen et al., 2006) could result in fluid oxidation and increase of HSO_4^-/H_2S ratio. The fluid oxidation would lead to the fractionation of heavy ^{34}S into the oxidized sulfur species because the ^{34}S-O bond is stronger than the ^{32}S-O bond, resulting in that residual ore-forming fluid becoming relatively ^{34}S-depleted and consequently producing ore-related pyrite characterized by negative $\delta^{34}S$ values (Ohmoto, 1986; Saunders et al., 1997). Thus, we propose that the negative $\delta^{34}S$ values for the S2 stage pyrite might result from the S isotope fractionation between sulfide and sulfate minerals via oxidation of ore-forming fluid (Ohmoto et al., 1972; Auhaber et al., 1978; Fan et al., 1994). This process was also genetically related to the extensive interaction between the ore-forming fluid and Fe^{2+}-rich andesite in the Xiong'er Group with the consumption of reduced S of the fluids during the pyrite formation (Lambert et al., 1984; Fan et al., 1994; Tang et al., 2013), as evidenced by the common alteration in and/or near the orebodies (Figs. 5a-b and 6a-c). However, the available data show that $\delta^{34}S$ values (−0.54 ~ 7.0‰) of barite in the ores from the Shanggong deposit are not very high (Chen and Fu, 1992; Lu et al., 2004). Considering the S isotope balance fraction between the sulfides and sulfates, suggesting the negative $\delta^{34}S$ values (−16.9 ~ -3.3‰ with an average of −10.9‰) of the S2 stage pyrite might not only result from S isotope fractionation (Chen et al., 2008; Ohmoto et al., 1972). The input of biogenic sulfur might also play an important role in forming the negative $\delta^{34}S$ values of the S2 stage pyrite (Chen et al., 2008; Ohmoto et al., 1972). Nevertheless, organic sulfur has not been discovered in any lithological units of the Xiong'ershan area (Tang et al., 2013), implying the negative $\delta^{34}S$ values unlikely mainly resulted from an organic sulfur source. Notably, Chen et al. (2008) suggested that the negative $\delta^{34}S$ values of ore-forming fluid in the S2 stage probably resulted from the input of biogenic sulfur in the Guandaokou and Luanchuan Groups exposed in the south of the Xiong'er Terrane during the continental collision between the YZB and NCC. However, the Guandaokou and Luanchuan Groups mainly consist of S-poor rocks (Tang, 2014) and have the $\delta^{34}S$ values of pyrite varying from −12.4‰ to 18.6‰ (Luo et al., 1991; Zhou et al., 1993), suggesting they were unlikely the major donator for the negative $\delta^{34}S$ (up to −16.9‰) of the S2 stage pyrite. Collectively, we propose that the negative $\delta^{34}S$ values of the S2 stage might result from both the S isotope fractionation between sulfides and sulfates and the input of biogenic sulfur of the Guandaokou and Luanchuan Groups.

The H-O isotopic results indicate that the S1 stage ore-forming fluid was mainly derived from magmatic-hydrothermal fluid, with meteoric water input in the S2 and S3 stages (Fan et al., 1998; Hu et al., 2013). Although intrusions that providing sufficient ore-forming fluids have not been discovered in the Shanggong deposit, gravity and magnetic geophysical investigations have suggested the existence of a concealed large pluton at ~ 3–5 km beneath the surface of the Shanggong deposit (Wang et al., 2019). Our LA-ICP-MS analyses show that the main ore-stage pyrite contains high contents of Au, As, Ag, Cu, Sb, Te, Tl, and Pb and shows a positive correlation between Au and the other elements (Fig. 9). The element association is consistent with that transported by magmatic aqueous vapor (Williams-Jones and Heinrich, 2005; Simon et al., 2005, Simon et al., 2006, Simon et al., 2007) and similar to that of

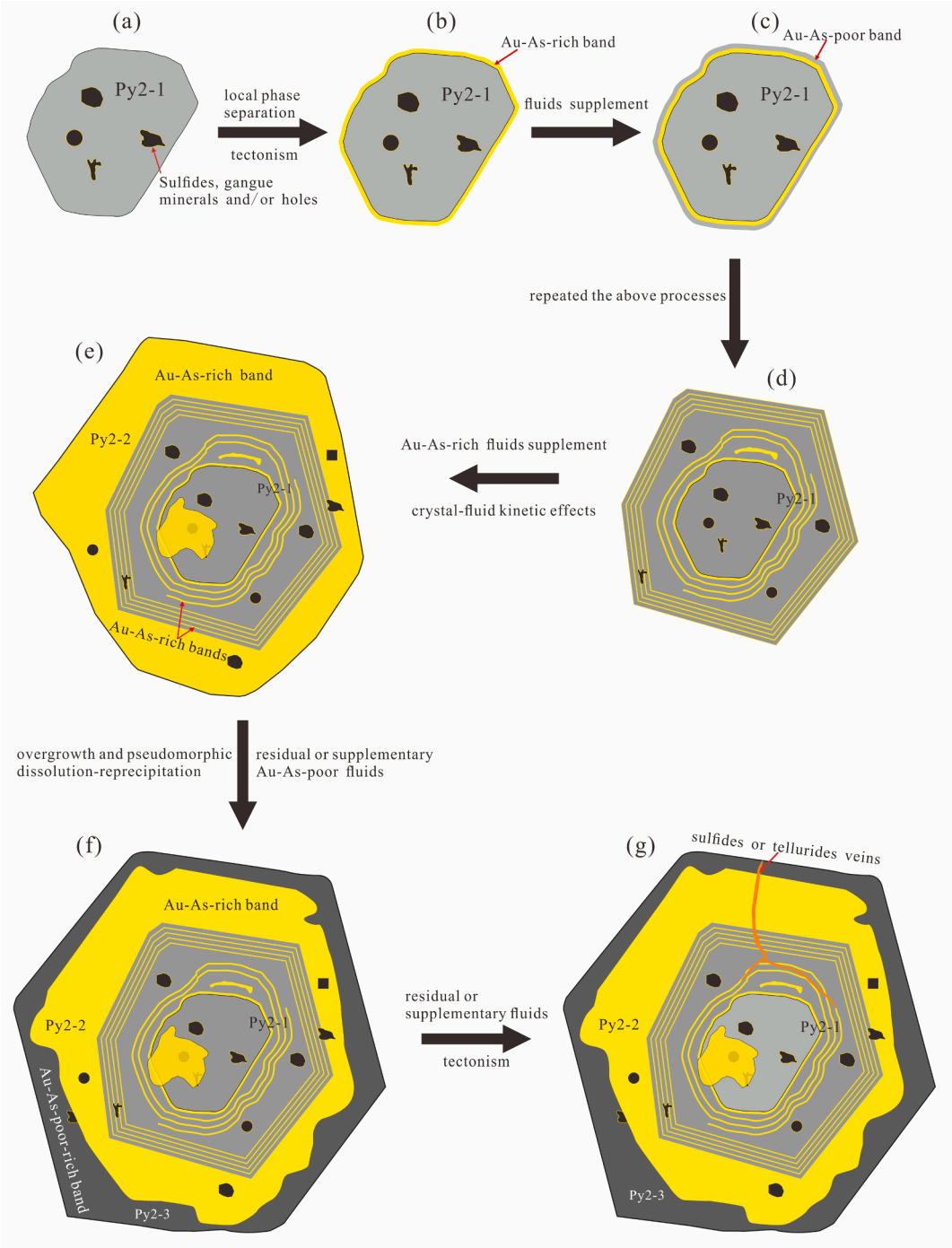

Fig. 13. Schematic diagram of the fluid pressure-driven zoned pyrite formation process during the S2 stage at the Shanggong deposit. See detailed explanations in the text.

the ore-stage pyrite from the Nevada's Carlin-type gold deposits with magmatic-origin (Muntean et al., 2011 and references therein). This suggests the ore-forming fluid was potentially sourced from magmatic-hydrothermal fluids. Furthermore, the main mineralization age (149.1 ± 6.7 Ma) is coincident with the ages of numerous Au, Mo, and Ag-Pb-Zn mineralization (163–113 Ma) and Late Mesozoic felsic and mafic magmas emplacement (158–112 Ma) in the southern NCC (Li et al., 2012a; Li et al., 2016; Zhao et al., 2018). These felsic magmas were derived from re-melting of ancient crystalline basement of the southern margin of the NCC with input of mantle materials (Gao and Zhao, 2017; Zhao et al., 2018), further supporting a magmatic source for the ore-forming fluid and materials. Apart from the abnormal sample 17SG71, the initial $^{87}Sr/^{86}Sr$ values recalculated at 149 Ma ($I_{Sr\text{-}149\ Ma}$) of sericite in the Shanggong deposit range from 0.7127 to 0.7162 with an average of 0.7141 (Appendix Table A5). This average is lower than the recalculated mean value of the Taihua Complex (0.7460, Appendix Table A5, Luan et al., 1985; Ni et al., 2012) and the Xiong'er Group (0.7238, Appendix Table A5, Peng et al., 2008; Zhao, 2000), but higher than that of the mantle (<0.706, Hu et al., 2013), suggesting the ore-forming materials were sourced from a mixture of crust and mantle. This conclusion is also evidenced by the Pb (Fan et al., 1994; Hu et al., 2013) and He-Ar isotopic results (Tang, 2014). In summary, we propose the Shanggong deposit could be potential of magmatic-hydrothermal origin with a mixed source of crust (e.g., the Taihua complex and

Xiong'er Group) and mantle for the ore-forming materials.

6. Conclusions

Gold mineralization in the Shanggong deposit is closely constrained in the NW-trending faults as breccia and altered rock-type ores. The timing of Au mineralization is constrained at 149.1 ± 6.7 Ma by Rb-Sr dating of ore-related sericite.

The S2 stage mineralization resulted from multiple pulses of hydrothermal fluids derived from a common sulfur source. Py2-1 with oscillatory zoning is interpreted to be the result of repeated local fluid phase separation at the near-surface of pyrite crystal due to sharp fluid pressure fluctuation. Py2-2 significantly enriched in Au and other metals should have resulted from both extrinsic (e.g., fluctuations in fluid pressure and composition) and intrinsic processes (e.g., local crystal-fluid kinetic effects. Then the exhausted ore-forming fluid was transported to the Py2-2-fluid interface, producing trace elements-poor Py2-3 and locally replacing Py2-2.

The Shanggong deposit is of possible magmatic origin for the initial ore-forming fluid and sulfur, and the ore-forming materials were sourced from both crust and mantle. The negative $\delta^{34}S$ values for the S2 stage pyrite might result from the S isotope fractionation in the ore-forming fluid and the input of biogenic sulfur of the Guandaokou and Luanchuan Groups.

Declaration of Competing Interest

The authors declare that they have no known competing financial interests or personal relationships that could have appeared to influence the work reported in this paper.

Acknowledgments

We thank Cheng Chen for his assistance with the field and the laboratory work. The authors acknowledge Yang Xiao for his help with LA-ICP-MS analyses. This work was financially supported by the Ministry of Science and Technology of the People's Republic of China (Grant Nos. 2016YFC0600106). We also appreciate editors and two anonymous reviewers for their constructive suggestions and comments.

Appendix A. Supplementary data

Supplementary data to this article can be found online at https://doi.org/10.1016/j.oregeorev.2022.104728.

References

Barker, S.L.L., Hickey, K.A., Cline, J.S., Dipple, G.M., Kilburn, M.R., Vaughan, J.R., Longo, A.A., 2009. Uncloaking invisible gold: use of nanosims to evaluate gold, trace elements, and sulfur isotopes in pyrite from carlin-type gold deposits. Econ. Geol. 104, 897–904.

Chen, Y.J., Fu, S.G., 1992. Gold Mineralization in West Henan, China. China Seismological Press, Beijing, p. 234 (in Chinese with English abstract).

Chen, Y.J., Pirajno, F., Sui, Y.H., 2004. Isotope geochemistry of the Tieluping silver-lead deposit, Henan, China: a case study of orogenic ssilver-dominated deposits and related tectonic setting. Miner. Depos. 39, 560–575.

Chen, Y.J., Zhao, Y.C., 1997. Geochemical characteristics and evolution of REE in the Early Precambrian sediment: evidences from the southern margin of the North China Craton. Episodes 20, 109–116.

Chen, Y.J., Pirajno, F., Qi, J.P., Li, J., Wang, H.H., 2006. Ore geology, fluid geochemistry and genesis of the Shanggong gold deposit, Eastern Qinling Orogen, China. Resour. Geol. 56, 99–116.

Chen, Y.J., Pirajno, F., Qi, J.P., 2008. The Shanggong gold deposit, Eastern Qinling Orogen, China, isotope geochemistry and implications for ore genesis. J. Asian Earth Sci. 33, 252–266.

Cox, S.F., 2016. Injection-driven swarm seismicity and permeability enhancement: implications for the dynamics of hydrothermal ore systems in high fluid-flux, overpressured faulting regimes-an invited paper. Econ. Geol. 111, 559–587.

Deditius, A.P., Utsunomiya, S., Ewing, R.C., Chryssoulis, S.L., Venter, D., Kesler, S.E., 2009. Decoupled geochemical behavior of As and Cu in hydrothermal systems. Geology 37, 707–710.

Deditius, A.P., Reich, M., Kesler, S.E., Utsunomiya, S., Chryssoulis, S.L., Walshe, J., Ewing, R.C., 2014. The coupled geochemistry of Au and As in pyrite from hydrothermal ore deposits. Geochim. Cosmochim. Acta 140, 644–670.

Dong, H.L., Hall, C.M., Peacor, D.R., Halliday, A.N., 1995. Mechanisms of argon retention in clays revealed by laser 40Ar-39Ar dating. Science 267, 355–359.

Fan, H.R., Xie, Y.H., Zhao, R., Wang, Y.L., 1994. Stable isotope geochemistry of rocks and gold deposits in the Xiong'ershan area western Henan province. Earth Sci. Front. 9 (1), 54–63 (in Chinese with English abstract).

Fan, H.R., Xie, Y.H., Wang, Y.L., 1998. Fluid-rock interaction during the mineralization process of the Shanggong structure-controlled alteration-type gold deposit in western Henan province, Central China. Acta Petrol. Sin. 14 (4), 529–541 (in Chinese with English abstract).

Faure, G., Mensing, T.M., 2005. Isotopes, Principles and Applications. Wiley, Hoboken, N.J., pp. 75–112

Fougerouse, D., Micklethwaite, S., Tomkins, A.G., Mei, Y., Kilburn, M., Guagliardo, P., Fisher, L.A., Halfpenny, A., Gee, M., Paterson, D., Howard, D.L., 2016a. Gold remobilization and formation of high-grade ore shoots driven by dissolution-reprecipitation replacement and Ni substitution into auriferous arsenopyrite. Geochim. Cosmochim. Acta 178, 143–159.

Fougerouse, D., Reddy, S.M., Saxey, D.W., Rickard, W.D.A., Riessen, A.V., Micklethwaite, S., 2016b. Nanoscale gold clusters in arsenopyrite controlled by growth rate not concentration: evidence from atom probe microscopy. Am. Mineral. 101, 1916–1919.

Gao, X.Y., Zhao, T.P., Yuan, Z.L., Zhou, Y.Y., Gao, J.F., 2010. Geochemistry and petrogenesis of the Heyu batholith in the southern margin of the North China block. Acta Petrol. Sin. 26, 3485–3506 (in Chinese with English abstract).

Gao, X.Y., Zhao, T.P., 2017. Late Mesozoic magmatism and tectonic evolution in the Southern margin of the North China Craton. Sci. China Earth Sci. 60, 1959–1975.

Guo, B., Zhu, L.M., Li, B., Gong, H.J., Wang, J.Q., 2009. Zircon U-Pb age and Hf isotope composition of the Huashan and Heyu granite plutons at the southern margin of North China Craton, implications for the geodynamic setting. Acta Petrol. Sin. 25, 265–281 (in Chinese with English abstract).

Han, Y.G., Zhang, S.H., Pirajno, F., Zhou, X.W., Zhao, G.C., Qü, W.J., Liu, S.H., Zhang, J. M., Liang, H.B., Yang, K., 2013. U-Pb and Re-Os isotopic systematics and zircon Ce4 +/Ce3+ ratios in the Shiyaogou Mo deposit in eastern Qinling, central China, insights into the oxidation state of granitoids and Mo (Au) mineralization. Ore Geol. Rev. 55, 29–47.

Hodkiewicz, P.F., Groves, D., Davidson, G.J., Weinberg, R.F., Hagemann, S.G., 2009. Influence of structural setting on sulphur isotopes in Archean orogenic gold deposits, Eastern Goldfields Province, Yilgarn, Western Australia. Mineral Deposita 44, 129–150.

Hu, X.L., He, M.C., Yao, S.Z., 2013. New understanding of the source of ore-forming material and fluid in the Shanggong gold deposit, East Qinling. Acta Geol. Sin. 87 (1), 91–100 (in Chinese with English abstract).

Huang, X.L., Wilde, S.A., Yang, Q.J., Zhong, J.W., 2012. Geochronology and petrogenesis of gray gneisses from the Taihua Complex at Xiong'er in the southern segment of the Trans-North China Orogen, implications for tectonic transformation in the Early Paleoproterozoic. Lithos 134–135, 236–252.

James-Smith, J., Cauzid, J., Testemale, D., Liu, W., Hazemann, J.L., Proux, O., Etschmann, B., Philippot, P., Banks, D., Williams, P., Brugger, J., 2010. Arsenic speciation in fluid inclusions using micro-beam X-ray absorption spectroscopy. Am. Mineral. 95, 921–932.

Kouzmanov, K., Pokrovski, G.S., 2012. Hydrothermal controls on metal distribution in porphyry Cu (-Au-Mo) systems. Soc. Econ. Geol. Spec. Pub. 16, 573–618.

Li, J.W., Bi, S.J., Selby, D., Chen, L., Vasconcelos, P., Thiede, D., Zhou, M.F., Zhao, X.F., Li, Z.K., Qiu, H.N., 2012a. Giant Mesozoic gold provinces related to the destruction of the North China craton. Earth Planet. Sci. Lett. 349, 26–37.

Li, X.H., Fan, H.R., Yang, K.F., Hollings, P., Liu, X., Hu, F.F., Cai, Y.C., 2018. Pyrite textures and compositions from the Zhuangzi Au deposit, southeastern North China Craton: implication for ore-forming processes. Contrib. Mineral. Petrol. 173, 9.

Li, J.W., Li, Z.K., Zhou, M.F., Chen, L., Bi, S.J., Deng, X.D., Qiu, H.N., Cohen, B., Selby, D., Zhao, X.F., 2012b. The Early Cretaceous Yangzhaiyu Lode Gold Deposit, North China Craton, a Link between craton reactivation and gold veining. Econ. Geol. 107 (1), 43–79.

Li, Z.K., Li, J.W., Cooke, D.R., Danyushevsky, L., Zhang, L., O'Brien, H., Lahaye, Y., Zhang, W., Xu, H.J., 2016. Textures, trace elements, and Pb isotopes of sulfides from the Haopinggou vein deposit, southern North China Craton, implications for discrete Au and Ag-Pb-Zn mineralization. Contrib. Mineral Petrol. 171, 99.

Liang, T., Lu, R., Luo, Z.H., Bai, F.J., Liu, X., 2015. LA-ICP-MS U-Pb Age of Zircons from Haopinggou Biotite Granite Porphyry in Xiong'er Mountain, Western Henan Province, and Its Geologic Implications. Geo Rev. 61 (4), 901–912 (in Chinese with English abstract).

Lu, X.X., Yu, X.D., Ye, A.W., 2003. Characteristics of ore-forming fluids in gold deposits of the Xiaoqinling-Xiong'ershan area. Mineral Deposits 22 (4), 377-385 (in Chinese with English abstract).

Lu, X.X., Yu, X.D., Dong, Y., Yu, Z.P., Chang, Q.L., Zhang, G.S., Liu, S.L., Ye, A.W., Suo, T. Y., Jin, J.P., 2004. The Characteristics of gold deposits and mantle fluids of Xiaoqinling-Xiong'ershan region. China Geological Publishing House, Beijing, 96 (in Chinese).

Luan, S.W., Cao, D.C., Fang, Y.K., Wang, J.Y., 1985. Geochemistry of the Xiao Qinling Mountains gold deposit. Mineral. Petrol. 5, 1–133 (in Chinese with English abstract).

Luo, M.J., Zhang, F.M., Dong, Q.Y., Xu, Y.R., Li, S.M., Li, K.H., 1991. Molybdenum Deposits in China. Science Technology Press, Zhengzhou, Henan, pp. 1–445.

Mao, J.W., Goldfarb, R.J., Zhang, Z.W., Xu, W.Y., Qiu, Y.M., Deng, J., 2002. Gold deposits in the Xiaoqinling-Xiong'ershan region, Qinling Mountains, central China. Miner. Deposita 37, 306–325.

Mao, J.W., Zheng, R.F., Ye, H.S., Gao, J.J., Chen, W., 2006. $^{40}Ar/^{39}Ar$ dating of fuchsite and sericite from altered rocks close to ore veins in Shagou large-size Ag–Pb–Zn deposit of Xiong'ershan area, western Henan Province, and its significance. Miner. Depos. 25, 359–368 (in Chinese with English abstract).
Mao, J.W., Xie, G.Q., Pirajno, F., Ye, H.S., Wang, Y.B., Li, Y.F., Zhao, H.J., 2010. Late Jurassic-Early Cretaceous granitoid magmatism in Eastern Qinling, central-eastern China, SHRIMP zircon U-Pb ages and tectonic implications. Austr. J. Earth Sci. 57 (1), 51–78.
Mao, J.W., Pirajno, F., Cook, N., 2011. Mesozoic metallogeny in East China and corresponding geodynamic settings: an introduction to the special issue. Ore Geol. Rev. 43 (1), 1–7.
Meffre, S., Large, R.R., Steadman, J.A., Gregory, D.D., Stepanov, A.S., Kamenetsky, V.S., Ehrig, K., Scott, R.J., 2016. Multi-stage enrichment processes for large gold-bearing ore deposits. Ore Geol. Rev. 76, 268–279.
Meng, L., Zhu, S.Y., Li, X.C, Chen, W.T., Xian, H.Y., Gao, X.Y., Zhao, T.P., 2021. Incorporation mechanism of structurally bound gold in pyrite: Insights from an integrated chemical and atomic-scale microstructural study. Am. Mineral., in press. doi:10.2138/am-2021-7812.
Mikucki, E.J., 1998. Hydrothermal transport and depositional processes in Archean lode-gold systems: a review. Ore Geol. Rev. 13, 307–321.
Muntean, J.L., Cline, J.S., Simon, A.C., Longo, A.A., 2011. Magmatic-hydrothermal origin of Nevada's Carlin-type gold deposits. Nat. Geosci. 4, 122–127.
Ni, Z.Y., Chen, Y.J., Li, N., Zhang, H., 2012. Pb-Sr-Nd isotope constraints on the fluid source of the the Dahu Au-Mo deposit in Qinling Orogen, central China, and impolication for Triassic tectonic setting. Ore Geol. Rev. 46, 60-67.
Ohmoto, H., 1986. Stable isotope geochemistry of ore deposits. Rev. Mineral. 16, 491–559.
Ohmoto, H., 1972. Systematics of sulfur and carbon isotopes in hydrothermal ore deposits. Econ. Geol. 67 (5), 551-578.
Peng, P., Zhai, M.G., Ernst, R.E., Guo, J.H., Liu, F., Hu, B., 2008. A 1.78 Ga large igneous province in the North China craton, the Xiong'er Volcanic Province and the North China dyke swarm. Lithos 101 (3–4), 260–280.
Perfetti, E., Pokrovski, G.S., Ballerat-Busserolles, K., Majer, V., Gibert, F., 2008. Densities and heat capacities of aqueous arsenious and arsenic acid solutions to 350°C and 300bar, and revised thermodynamic properties of $As(OH)_3^\circ$(aq), $AsO(OH)_3^\circ$ (aq) and iron sulfarsenide minerals. Geochim. Cosmochim. Acta 72, 713–731.
Peterson, E.C., Mavrogenes, J.A., 2014. Linking high-grade gold mineralization to earthquake-induced fault-valve processes in the Porgera gold deposit, Papua New Guinea. Geology 42, 383–386.
Putnis, A., 2002. Mineral replacement reactions: from macroscopic observations to microscopic mechanisms. Mineral. Mag. 66, 689–708.
Putnis, A., Fernandez-Diaz, L., Prieto, M., 1992. Experimentally produced oscillatory zoning in the $(Ba, Sr)SO_4$ solid solution. Nature 358, 743–745.
Saunders, J.A., Pritchett, M.A., Cook, R.B., 1997. Geochemistry of biogenic pyrite and ferromanganese coatings from a small watershed, a bacterial connection? Geomicrobiol. J. 14, 203–217.
Simon, A.C., Frank, M.R., Pettke, T., Candela, P.A., Piccoli, P.M., Heinrich, C.A., 2005. Gold partitioning in melt-vapor-brine systems. Geochim. Cosmochim. Acta 69, 3321–3335.
Simon, A.C., Pettke, T., Candela, P.A., Piccoli, P.M., Heinrich, C.A., 2006. Copper partitioning in a melt-vapor-brine-magnetite-pyrrhotite assemblage. Geochim. Cosmochim. Acta 70, 5583–5600.
Simon, A.C., Pettke, T., Candela, P.A., Piccoli, P.M., Heinrich, C.A., 2007. The partitioning behavior of As and Au in S-free and S-bearing magmatic assemblages. Geochim. Cosmochim. Acta 71, 1764–1782.
Tang, L., Hu, X.K., Santosh, M., Zhang, S.T., Spencer, C.J., Jeon, H., Zhao, Y., Cao, H.W., 2019. Multistage processes linked to tectonic transition in the genesis of orogenic gold deposit: a case study from the Shanggong lode deposit, East Qinling, China. Ore Geol. Rev. 111.
Tang, K.F., Li, J.W., Selby, D., Zhou, M.F., Bi, S.J., Deng, X.D., 2013. Geology, mineralization, and geochronology of the Qianhe gold deposit, Xiong'ershan area, southern North China Craton. Miner Depos. 48 (6), 729–747.
Tang, K.F., 2014. Characteristics, genesis, and geodynamic setting of representative gold deposits in the Xiong'ershan district, southern margin of the North China Craton. Doctoral Dissertation. Geol. J. China Univ., Wuhan, pp. 1-162 (in Chinese with English abstract).
Wang, J.H., Wang, A., Wang, Y.S., Qin, X.Y., Chen, S.M., 2019. Characteristics of gravity and magnetic fields and deep metallogenic prediction in the Xiong'ershan area, western Henan province. Geol. Bull. China 39 (5), 735–745.
Wang, Y., Xu, H., Merino, E., Konishi, H., 2009. Generation of banded iron formations by internal dynamics and leaching of oceanic crust. Nat. Geosci. 2, 781–784.
Watson, E.B., 2004. A conceptual model for near-surface kinetic controls on the trace-element and stable isotope composition of abiogenic calcite crystals. Geochim. Cosmochim. Acta 68, 1473–1488.
Williams-Jones, A.E., Heinrich, C.A., 2005. Vapor transport of metals and the formation of magmatic-hydrothermal ore deposits. Econ. Geol. 100, 1287–1312.
Wu, Y.F., Li, J.W., Evans, K., Koenig, A.E., Li, Z.K., O'Brien, H., Lahaye, Y., Rempel, K., Hu, S.Y., Zhang, Z.P., Yu, J.P., 2018. Ore-Forming Processes of the Daqiao Epizonal Orogenic Gold Deposit, West Qinling Orogen, China: constraints from textures, trace elements, and sulfur isotopes of pyrite and marcasite, and Raman spectroscopy of carbonaceous material. Econ. Geol. 113, 1093–1132.
Wu, Y.F., Fougerouse, D., Evans, K., Reddy, S.M., Saxey, D.W., Guagliardo, P., Li, J.W., 2019. Gold, arsenic, and copper zoning in pyrite: a record of fluid chemistry and growth kinetics. Geology 47, 641–644.
Xiao, E., Hu, J., Zhang, Z.Z., Dai, B.Z., Wang, Y.F., Li, H.Y., 2012. Petrogeochemistry, zircon U-Pb dating, and Lu-Hf isotopic compositions of the Haoping and Jinshanmiao granites from the Huashan complex batholith in eastern Qinling Orogen. Acta Petrol. Sin. 28 (12), 4031–4046 (in Chinese with English abstract).
Xing, Y.L., Brugger, J., Tomkins, A., Shvarov, Y.R., 2019. Arsenic evolution as a tool for understanding formation of pyritic gold ores. Geology 47, 335–338.
Xu, W.G., Fan, H.R., Hu, F.F., Santosh, M., Yang, K.F., Lan, T.G., Wen, B.J., 2014. Gold mineralization in the Guilaizhuang deposit, southwestern Shandong Province, China, insights from phase relations among sulfides, tellurides, selenides and oxides. Ore Geol. Rev. 56, 276–291.
Zhang, Z.H., Zhang, J.X., Ye, S.Z., 1994. Isotope Dating on Au Deposits in East Shandong. China Seismological Press, Beijing, pp. 56 (In Chinese).
Zhang, J.C., Lin, Y.T., Yang, W., Shen, W.J., Hao, J.L., Hu, S., Cao, M.J., 2014. Improved precision and spatial resolution of sulfur isotope analysis using NanoSIMS. J. Anal. At. Spectrom. 29, 1934–1943.
Zhang, X.M., Spay, P.G., 1994. Calculated stability of aqueous Te species, calaverite, and hessitc at elevated temperatures. Econ. Geol. 89, 1152–1166.
Zhao, G.C., Cawood, P.A., 2012. Precambrian geology of China. Precambr. Res. 222, 13–54.
Zhao, T.P., Zhai, M.G., Xia, B., Li, H., Zhang, Y., Wan, Y., 2004. Zircon U-Pb SHRIMP dating for the volcanic rocks of the Xiong'er Group, constraints on the initial formation age of the cover of the North China Craton. Chin. Sci. Bull. 49, 2495–2502.
Zhao, T.P., Meng, L., Gao, X.Y., Jin, C., Wu, Q., Bao, Z.W., 2018. Late Mesozoic felsic magmatism and Mo-Au-Pb-Zn mineralization in the southern margin of the North China Craton. A review. J. Asian Earth Sci. 161, 103–121.
Zhao, T.P., 2000. The characteristic and genesis of proterozoic potassic volcanic rock in southern margin of the North plate. Docter dissertation, Institute of geology and Geophysis, Chinese Academy of Science, Beijing, 102 (In Chinese with English abstract).
Zheng, J.P., Dai, H.K., 2018. Subduction and retreating of the western Pacific plate resulted in lithospheric mantle replacement and coupled basin-mountain respond in the North China Craton. Sci. China Earth Sci. 61, 406–424.
Zheng, Y.F., Xu, Z., Zhao, Z.F., Dai, L.Q., 2018. Mesozoic mafic magmatism in North China, Implications for thinning and destruction of cratonic lithosphere. Sci. China Earth Sci. 61, 353–385.
Zhou, Z.J., Chen, Y.J., Jiang, S.Y., Hu, C.J., Qin, Y., Zhao, H.X., 2015. Isotope and fluid inclusion geochemistry and genesis of the Qiangma gold deposit, Xiaoqinling gold field, Qinling Orogen, China. Ore Geol. Rev. 66, 47–64.
Zhou, Z.X., Li, B.L., Guo, K.H., Zhao, R., Xie, Y.H., 1993. Genesis of the Gold (Molybdeum) Deposits in Southern Margin of the Northern China Craton. Seismological Press, Beijing, pp. 1–259 (in Chinese).
Zhu, R.X., Fan, H.R., Li, J.W., Meng, Q.R., Li, S.R., Zeng, Q.D., 2015. Decratonic gold deposits. Sci. China-Earth Sci. 58, 1523–1537.